物 理 化 学 学 报

Acta Phys. -Chim. Sin. **2021,** *37* (6), 2010017 (1 of 31)

[Review] doi: 10.3866/PKU.WHXB202010017 www.whxb.pku.edu.cn

Review of Z-Scheme Heterojunctions for Photocatalytic Energy Conversion

Dong Liu, Shengtao Chen, Renjie Li *, Tianyou Peng *

College of Chemistry and Molecular Sciences, Engineering Research Center of Organosilicon Compounds & Materials, Ministry of Education, Wuhan University, Wuhan 430072, China.

Abstract: Inspired by the photosynthesis of green plants, various artificial photosynthetic systems have been proposed to solve the energy shortage and environmental problems. Water photosplitting, carbon dioxide photoreduction, and nitrogen photofixation are the main systems that are used to produce solar fuels such as hydrogen, methane, or ammonia. Although conducting artificial photosynthesis using man-made semiconducting materials is an ideal and potential approach to obtain solar energy, constructing an efficient photosynthetic system capable of producing solar fuels at a scale and cost that can compete with fossil fuels remains challenging. Therefore, exploiting the efficient and low-cost photocatalysts is crucial for boosting the three main photocatalytic processes (light-harvesting, surface/interface catalytic reactions, and charge generation and separation) of artificial photosynthetic systems. Among the various photocatalysts developed, the Z-scheme heterojunction composite system can increase the light-harvesting ability and remarkably suppress charge carrier recombination; it can also promote surface/interface catalytic reactions by preserving the strong reductive/oxidative capacity of the photoexcited electrons/holes, and therefore, it has attracted considerable attention. The continuing progress of Z-scheme nanostructured heterojunctions, which convert solar energy into chemical energy through photocatalytic processes, has witnessed the importance of these heterojunctions in further improving the overall efficiency of photocatalytic reaction systems for producing solar fuels. This review summarizes the progress of Z-scheme heterojunctions as photocatalysts and the advantages of using the direct Z-scheme heterojunctions over the traditional type II, all-solid-state Z-schemel, and liquid-phase Z-scheme ones. The basic principle and corresponding mechanism of the two-step excitation are illustrated. In particular, applications of various types of Z-scheme nanostructured materials (inorganic, organic, and inorganic-organic hybrid materials) in photocatalytic energy conversion and different controlling/engineering strategies (such as extending the spectral absorption region, promoting charge transfer/separation and surface chemical modification) for enhancing the photocatalytic efficiency in the last five years are highlighted. Additionally, characterization methods (such as sacrificial reagent experiment, metal loading, radical trapping testing, *in situ* X-ray photoelectron spectroscopy, photocatalytic reduction experiments, Kelvin probe force microscopy, surface photovoltage spectroscopy, transient absorption spectroscopy, and theoretical calculation) of the Z-scheme photocatalytic mechanism, and the assessment criteria and methods of the photocatalytic performance are discussed. Finally, the challenges associated with Z-scheme heterojunctions and the possible growing trend are presented. We believe that this review will provide a new understanding of the breakthrough direction of photocatalytic performance and provide guidance for designing and constructing novel Z-scheme photocatalysts.

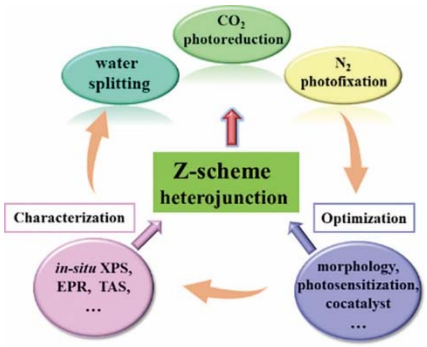

Key Words: Semiconductor; Photocatalysis; Z-scheme heterojunction; Energy conversion; Reaction mechanism

Received: October 11, 2020 ; Revised: November 13, 2020; Accepted: November 16, 2020; Published online: November 26, 2020.

*Corresponding authors. Emails: lirj@whu.edu.cn (R.L.); typeng@whu.edu.cn (T.P.). Tel.: +86-27-68752237 (R.L.); +86-27-68752237 (T.P.).

This work is supported by the Natural Science Foundation of China (21975190, 21871215, 21631003, 21573166), the Science & Technology Planning Project of Shenzhen Municipality, China (JCYJ20180302153921190), Natural Science Foundation of Jiangsu Province, China (BK20151247), and the Funds for Creative Research Groups of Hubei Province, China (2014CFA007)

国家自然科学基金(21975190, 21871215, 21631003, 21573166)、深圳市科技创新委员会科技项目(JCYJ20180302153921190)、江苏省自然科学基金(BK20151247)、湖北省创新群体(2014CFA007)资助项目

用于光催化能量转换的 Z-型异质结的研究进展

刘东，陈圣韬，李仁杰*，彭天右*

武汉大学化学与分子科学学院,有机硅化合物及材料教育部工程研究中心，武汉 430072

摘要：受植物光合作用的启发，研究者发展了多种模拟光合作用体系用于光分解水、二氧化碳光还原和氮光固定以生产“太阳燃料”(如氢气、甲烷和氨气)，以期缓解当前的能源短缺和环境污染。尽管基于人造半导体材料的光合作用是一种潜在、理想的以“太阳燃料”的化学键形式存储太阳能的方法，但是构筑能够在规模和成本方面与化石燃料竞争的生产“太阳燃料”的人工光合作用体系仍然存在巨大的挑战。因此，开发低成本的高效光催化剂对于促进人工光合作用的三种主要光催化过程(光俘获、电荷产生与分离，以及表面/界面催化反应)具有重要的意义。在已研究的各类光催化剂中，Z-型异质结复合体系不仅可以提高光俘获能力和显著抑制电荷载流子复合，而且还可通过保持光激发电子/空穴的强还原/氧化能力来促进表面/界面催化反应，因而受到广泛关注。将太阳能转化为化学能的 Z-型纳米异质结的研究证明这些异质结在提高生产“太阳燃料”的光催化反应体系的整体效率方面的重要性。该综述主要介绍了 Z-型异质结的发展历史和直接 Z-型异质结相较于传统 II 型异质结、液相 Z-型和全固态 Z-型异质结的优势，并阐述了两步激发 Z-型光催化体系的反应机理和途径。然后，从材料组成角度重点介绍了近 5 年来不同类型 Z-型纳米结构材料(无机，有机和无机-有机复合材料)在光催化能源转换领域的应用，以及提高 Z-型纳米结构材料光催化性能的各种调控/工程策略(如扩展光谱吸收区、促进电荷转移/分离和表面化学改性等)。此外，还讨论了 Z-型光催化机理的表征方法与策略(如金属负载法、牺牲试剂测试法、自由基捕集实验、原位 X-射线光电子能谱、光催化还原实验、Kelvin 探针力显微镜、表面光电压光谱、瞬态吸收光谱及理论计算等)及光催化性能的评价方法和标准。最后，介绍了 Z-型异质结光催化体系目前面临的挑战和发展方向。我们希望该综述能为光催化体系的性能突破方向提供新的认识，并为新型 Z-型光催化材料的设计和构筑提供指导。

关键词：半导体；光催化；Z-型异质结；能源转化；反应机理

中图分类号：O643

1 Introduction

Since the first progress of photoelectrochemical water splitting over titania (TiO_2) electrode under ultraviolet (UV) light was reported by Fujishima and Honda [1], significant progress have been made to the development of photoactive semiconductor and its corresponding photocatalytic reaction systems that convert the abundant but intermittent solar energy into chemical energy. The corresponding photocatalytic energy conversion systems based on man-made semiconducting materials mainly include water photosplitting into hydrogen (H_2) and/or oxygen (O_2), carbon dioxide (CO_2) photoreduction to solar fuels such as methane (CH_4), methanol (CH_3OH), ethanol (C_2H_5OH) and formic acid (HCOOH), and nitrogen (N_2) photofixation to ammonia (NH_3). Generally, there are three main steps in the photocatalytic process: (1) Light absorption. The photogenerated electrons from the valence band (VB) will be excited to the conduction band (CB) if the incident light energy is equal to or greater than the bandgap energy (E_g) of the semiconductor to create the hole-electron pairs [2]; (2) Charge transfer and separation. The photogenerated charge carriers (electrons and holes) migrate to the semiconductor surface; (3) Surface redox reactions. Those oxidative holes and reductive electrons initiate the reduction and oxidation reactions on the semiconductor surface, respectively. The evolution and separation of photogenerated charge of semiconductor are the determining factors to the performance.

Dr. Renjie Li received his BS in applied chemistry in 2003 and his Ph.D. in inorganic chemistry in 2008 from Shandong University. He joined the faculty of Wuhan University in 2008 and is now an associate professor. He currently works on solar cells and photocatalysis using the functional materials, such as the phthalocyanines and porphyrins.

Prof. Tianyou Peng received his Ph.D. degree in Chemistry from Wuhan University, China in 1998. He did a post-doc at Kyoto University, Japan with Prof. K. Hirano. He has been a full Professor at College of Chemistry and Molecular Sciences of Wuhan University since 2004. Right now, he is the Director of the Institute of Inorganic Chemistry in Wuhan University. His scientific interests are in inorganic chemistry, material chemistry, and nanomaterials including dye-sensitized solar cell and clean energy production including photocatalytic H_2 production, CO_2 conversion and N_2 fixation.

As well known, the single-component photocatalyst with a narrow bandgap hardly satisfies all of the above requirements because of the fast photogenerated charge recombination and undesirable redox capacity. In contrast, wide bandgap semiconductor photocatalysts cannot effectively capture the solar light, and thus the single-component photocatalysts usually display low photocatalytic capability [3]. Fortunately, composite materials as photocatalysts present some potential advantages. For example, the band bending of the two semiconductors in type II heterojunction can lead to the migration of charge carriers in the opposite direction because of their different chemical potentials [4], which can remarkably enhance the spatial separation of hole-electron pairs. Nevertheless, traditional type II heterojunction has a primary defect. The oxidation and reduction ability of the charge carriers are weakened upon the charge transfer process, whereby the CB electrons in semiconductor will transfer to the less negative CB of another, and the VB holes will migrate to the VB with less positive potential of another, ultimately, the redox capability of charge carriers are lowered. Besides, the electrostatic repulsion between the holes and holes (electrons and electrons) would also retard the continuous transfer of the oxidative VB-holes and reductive CB-electrons between the two semiconductors [5]. These issues in the conventional type II heterojunction can be surmounted by a Z-scheme system, in which the VB-holes and CB-electrons possessing inferior redox ability will recombine. At the same time, the stronger oxidative VB-holes and reductive CB-electrons are preserved in the respective semiconductors. This charge transfer path can retain redox charge carriers to drive the photocatalytic reaction and improve the semiconductor's charge separation. Consequently, the photocatalytic performance of Z-scheme heterojunction is usually better than of type II heterojunction and single-component photocatalyst [6].

The term "Z-scheme" derives from the electron transfer path following a letter "Z" in the natural photosynthetic system of green plants, which consists of two components, that is, photosystem (PS) I and PS II [7]. Artificial Z-scheme photocatalytic systems (two-step excitation) are designed, whereby two semiconductors are used to replace the PS I and PS II [8,9]. The pioneering work of Z-scheme system was introduced by Bard (Fig. 1) [10], where different semiconductors were connected by a shuttle redox mediator to form liquid-phase Z-scheme system (the first generation in Fig. 1) [11]. The shuttle redox mediator (such as IO_3^-/I^-, Fe^{3+}/Fe^{2+}, $[Co(bpy)_3]^{3+/2+}$, and $[Co(phen)_3]^{3+/2+}$) can boost the photogenerated electrons transporting from the CB of PS I to the VB of PS II. However, liquid-phase Z-scheme system has the restriction of the redox mediator's reversibility and light-shielding effect as well as its application range limited to liquid-phase reactions. This deficiency triggered the evolution of next generation Z-scheme system. In 2006, Tada *et al*. [12] introduced the all-solid-state Z-scheme photocatalyst (the second generation in Fig. 1) that consists of two different semiconductors with a conductor (such as Ag, Au, Ir noble metals) as electron mediator. This all-solid-state Z-scheme photocatalyst is appropriate for both gas phase and liquid phase reaction. Without the ion redox mediator, the backward reaction and light-shielding effect in the liquid-phase Z-scheme systems can be inhibited [13–15], which can give low resistance *via* Ohmic contact. The noble metal electron mediator can also be replaced with other conductive materials, such as graphene, carbon nanotubes (CNTs), carbon quantum dots (CQDs), *etc*. [16] Nevertheless, the noble metals is expensive and the complex components restrict the widespread utilization of the solid-state Z-scheme photocatalysts. In 2013, Yu *et al*. [17] found that the conductive layer is not necessary if two semiconductors can be consistent with their CB and VB positions, and reported a direct Z-scheme photocatalyst (the third generation in Fig. 1) by combining g-C_3N_4 and TiO_2, whereby PS I and PS II should have suitable energy band structures, and the CB potential of PS II should be more negative than the VB potential of PS I. Usually, a direct Z-scheme photocatalyst have two semiconductors with a direct contact at their interface. Under light illumination, the photogenerated electrons in the CB of PS II will transfer to the interface and recombine with the holes in the VB of PS I due to the intense electrostatic attraction, and thus the holes and electrons with stronger reductive and oxidative ability can be preserved in the CB of PS I and the VB of PS II, respectively. Another key factor for constructing a direct Z-scheme photocatalyst is the solid-solid contact interface of PS I and II, and matched band structure and confidential contact (physical contact or chemical bonding) between the two semiconductors would facilitate the direct electron transfer and lower the transfer distance of charge carriers without the assistance of electron mediator, thus causing remarkably reduced construction cost and eliminated light-shielding effect.

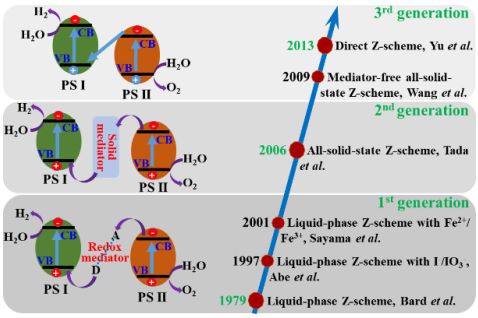

Fig. 1 The evolution roadmap of Z-scheme photocatalytic system and the mechanisms of liquid-phase, all-solid-state and direct Z-scheme systems.

The above-mentioned each type of Z-scheme system owns its advantages and disadvantages. For example, the liquid-phase system gives the PS development's flexibility due to the isolated units, but are limited by the backward reaction and light-shielding effect. All-solid-state system renders more conditions for Z-schematic reactions, however, expensive nanocarbon or metallic electron mediator is required, and the formation of a direct Z-scheme system is the same to the nature of PS units,

which lacks the flexibility in material selection.Moreover, Z-scheme systems can supply larger driving force to alleviate the thermodynamic requirement for the photocatalytic energy conversion processes. In view of the above advantages, this work will talk about the components of Z-scheme photocatalysts, reaction mechanism and application in the water photosplitting, CO_2 photoreduction and N_2 photofixation for providing some guidance to the further researches on highly efficient photocatalytic energy conversion through Z-scheme mechanism [18,19].

2 Basic principle, mechanism and performance evaluation

2.1 Basic principle and mechanism of Z-scheme system

Typically, Z-scheme heterojunction can be fabricated by the hybridization of an oxidative semiconductor (PS II) with sufficient positive VB position and a reductive one (PS I) with enough negative CB position. Under the irradiation, the electrons in the CB of oxidative semiconductor are photogenerated and migrated to the interface and recombine with the photogenerated holes in the VB of reductive one, consuming the relatively inactive charge carriers [20–22]. To enhance the energy conversion efficiency, some subjects should be solved for the components of Z-scheme system [23]: (1) VB/CB positions. The reductive semiconductor should have the CB position high enough and the oxidative one should have the VB position deep enough. Also, it is desired that a staggered type must be formed to promote the separation of the photoexcited charge carriers and the spatial isolation of the redox reactions as well as their products. (2) Light-harvesting capability. Most wide bandgap semiconductors such as TiO_2, ZnO and $SrTiO_3$ feature weak light-harvesting capability, a general approach for fabricating Z-scheme heterojunctions is combining the wide bandgap semiconductor with a narrow one for promoting the light harvesting. In addition, the multiple light scattering and reflection of hierarchical structures such as nanoflower, hollow microsphere and porous material can also boost the light harvesting [7,24]. (3) Charge transfer and separation. Apart from the appropriate energy level alignment and a wide range of solar light harvesting, fast charge migration is crucial for Z-scheme heterostructure as well. In this case, the migration efficiency of charge carriers strongly relies on the resistance of transfer path, diffusion distance and transfer rate. Hence, reducing the transfer distance and interface resistance should be taken into consideration in designing Z-scheme heterostructure.

What's more, the contact interface imposes important effect on the resistance, and thus large efforts have been devoted to improving the interface from many factors, such as adopting *in situ* preparation methods to achieve the intimate contact between the two semiconductors, lowering the lattice mismatch by applying materials with the similar ions or lattice parameters. Furthermore, the morphology, crystal facets, and particle size should be modified to reduce the charge migration distance [24–27]. In general, the above principles are suitable for various Z-scheme photocatalytic systems including water splitting, CO_2 reduction, N_2 fixation, pollutant degradation and so forth. This section will mainly introduce the basic principle and mechanism of Z-scheme systems for water photosplitting, CO_2 photoreduction and N_2 photofixation for shedding light on the progress of highly efficient photocatalytic energy conversion systems *via* Z-scheme mechanism.

2.1.1 Water photosplitting

Hydrogen (H_2) as one renewable energy has attracted much interest of researchers, and water photosplitting to produce H_2 and/or O_2, that is, artificial photosynthesis, has been a hot-pot and bears lots of merits such as inexhaustible light source (solar energy), low cost, nonpolluting reaction, high energy density and simple reaction facility [18,19,28–30]. Generally, a desirable active semiconductor should meet the crucial requirements as follows [31,32]: (1) Ideal bandgap energy (E_g) should be 1.5–3.2 eV for efficiently utilizing the solar light. The semiconductors with an E_g smaller than 1.5 eV cannot supply sufficient driving force to overcome the overpotentials existing in the photocatalytic reactions, while the semiconductor with an E_g larger than 3.2 eV cannot efficiently harvest sunlight. (2) CB minimum (CBM) should be more negative than the water reduction potential and VB maximum (VBM) should be more positive than the water oxidation level. (3) Surface area, reactive or porosity facets should be larger for active sites. (4) Stability in both basic and acidic medium. (5) Photocorrosion against resistance. Since it's tough for a single-component semiconductor to satisfy all the above requirements, constructing Z-scheme heterojunction can broaden the light adsorption range, lower the energy band requirement and separate the charge carriers in two different semiconductors. Therefore, utilizing a reductive semiconductor and an oxidative one to construct Z-scheme heterojunction is a fascinating approach to obtaining high-efficiency water splitting system.

Actually, water splitting process consists of two half reactions together with the full reaction of water splitting (Eq. 3): H_2 evolution half reaction (HER, Eq. 1) and O_2 evolution half reaction (OER, Eq. 2). It's worth noting that the use of sacrificial electron donor, such as triethanolamine (TEOA), methanol (CH_3OH), ethanol (C_2H_5OH), ascorbic acid (AA) or electron acceptor (such as silver nitrate ($AgNO_3$), ferric chloride ($FeCl_3$), can improve the HER or OER half reactions, while the overall water splitting ($\Delta G^0 = 237.13$ kJ·mol^{-1}) is no need of the above sacrificial reagents. Those half and overall reactions of water splitting and the related reduction potentials (V *vs.* NHE at pH 7.0) can be summarized as follows [23,33–36]:

$$2H^+ + 2e^- \rightarrow H_2 \qquad E = -0.42\ \text{V} \qquad (1)$$

$$2H_2O + 4h^+ \rightarrow O_2 + 4H^+ \qquad E = +0.81\ \text{V} \qquad (2)$$

$$H_2O = H_2 + 1/2O_2 \qquad E = +1.23\ \text{V} \qquad (3)$$

2.1.2 CO_2 photoreduction

Large amount of anthropogenic CO_2 emission associated with

the increasing fossil fuel consumption has aroused the issues of the energy crisis and global warming. CO_2 photoreduction into solar fuels, such as CH_4, CH_3OH, C_2H_5OH and HCOOH, is a promising method to address those problems [37]. Due to the high energy input to break C=O bond (750 kJ·mol^{-1}) compared with that of C−O (327 kJ·mol^{-1}), C−C (336 kJ·mol^{-1}) and C−H (411 kJ·mol^{-1}) and the fairly large energy gap (*ca.* 13.7 eV) between its lowest unoccupied molecular orbital (LUMO) and highest occupied molecular orbital (HOMO), CO_2 is one of the most stable molecules thermodynamically [38,39], and therefore CO_2 photoreduction is a great challenge. As is known, CO_2 photoreduction is a heterogeneous catalytic process, inevitably involving the absorption and activation of CO_2, which are not the dominant topic of this review and can be referred to some other reviews [40,41]. The chemisorption of CO_2 on photocatalysts is the initial step to rearrange the geometry structure of CO_2 from liner to bent structure (CO_2^-) *via* a single-electron reduction process [42,43], and the potential of CO_2/CO_2^- couple is −1.90 V (*vs.* NHE, at pH = 7.0，Eq. 4) [44], which is too high to complete the reaction from the thermodynamical aspect. To surmount the difficulty of the single-electron reaction, more favorable proton-assisted multielectron transfer route was proposed, which can reduce the thermodynamic potential requirement for the CO_2 reduction reactions as depicted in Eqs. 5–9 (*vs.* NHE, at pH 7.0) [45].

$$CO_2 + e^- = CO_2^- \quad E^\ominus = -1.90\ V \quad (4)$$
$$CO_2 + 2H^+ + 2e^- = HCOOH \quad E^\ominus = -0.61\ V \quad (5)$$
$$CO_2 + 2H^+ + 2e^- = CO + H_2O \quad E^\ominus = -0.53\ V \quad (6)$$
$$CO_2 + 4H^+ + 4e^- = HCHO + H_2O \quad E^\ominus = -0.48\ V \quad (7)$$
$$CO_2 + 6H^+ + 6e^- = CH_3OH + H_2O \quad E^\ominus = -0.38\ V \quad (8)$$
$$CO_2 + 8H^+ + 8e^- = CH_4 + 2H_2O \quad E^\ominus = -0.24\ V \quad (9)$$
$$H_2O + h^+ = \cdot OH + H^+ \quad E^\ominus = +2.31\ V \quad (10)$$
$$O_2 + e^- = O_2^- \quad E^\ominus = -0.137\ V \quad (11)$$

When H_2O is added and served as reducing reagent in the CO_2 photoreduction system (Eqs. 10,11), H_2 can originate from H_2O (Eq. 1). Therefore, the contest between water reduction toward H_2 and CO_2 reduction toward hydrocarbons is inevitable. In order to increase the CO_2 photoreduction efficiency, the formation of H_2 is desired to be as low as possible.

2.1.3 N_2 photofixation

Nitrogen is one of the earth abundant elements, mostly as nitrogen gas (N_2) in atmosphere. N_2 reduction to NH_3 is essential because it is significant to human society. Moreover, NH_3 has been named as an easily transportable “energy store” for new energy. Haber-Bosch process, as the typical industrial nitrogen fixation method, always conducts under high temperature and pressure conditions, and requires large amount input of hydrogen and energy source [46,47]. While the efficiency of Haber-Bosch process is limited to about 15% [48]. Hence, numerous researches have been devoted to the development of N_2 photofixation. The pioneering study on TiO_2-based photocatalysts for N_2 fixation was reported by Schrauzer and Guth in 1977 [49], in which Fe-doped TiO_2 was used to reduce N_2 to NH_3 under UV irradiation. Since then, N_2 photofixation has caused increasingly attention [50]. Since the driving force (light) and ingredients (water and air) are environmentally friendly, low cost and accessible, N_2 photofixation has attracted increasing attention and achieved great advance in recent years.

The basic principle for N_2 photofixation is alike to the above-mentioned photocatalytic reaction mechanism for water splitting and CO_2 reduction. The typically accepted mechanisms of N_2 photofixation to NH_3 is displayed in Fig. 2. In the alternating pathway, four hydrogenation steps are used to form hydrazine bounds between the N atoms of the N_2 molecule, which are hydrogenated alternately. The fifth step will release the first NH_3 molecule [51]. In the distal pathway, a single N atom of N_2 molecule is hydrogenated using three steps after the first NH_3 is released, and a second NH_3 will be produced after the remaining nitride-N conducting three more hydrogenation steps. The difference lies in the reductive reactions, N_2 is reduced to NH_3 with the assistance of water-derived protons in N_2 photofixation process, which requires six electrons for reductive one N_2 molecule. The hydrogenation reactions of the above process and the related reduction potentials (V *vs.* NHE at pH 7.0) can be summarized as Eqs. 12–18 (*vs.* NHE, at pH 0.0) [23,33–55]:

$$N_2 + e^- = N_2^- \quad E^\ominus = -4.16\ V \quad (12)$$
$$N_2 + H^+ + e^- = N_2H \quad E^\ominus = -3.20\ V \quad (13)$$
$$N_2 + 2H^+ + 2e^- = N_2H_2 \quad E^\ominus = -1.10\ V \quad (14)$$
$$N_2 + 4H^+ + 4e^- = N_2H_4 \quad E^\ominus = -0.36\ V \quad (15)$$
$$N_2 + 5H^+ + 4e^- = N_2H_5^+ \quad E^\ominus = -0.23\ V \quad (16)$$
$$N_2 + 6H^+ + 6e^- = 2NH_3 \quad E^\ominus = +0.55\ V \quad (17)$$
$$N_2 + 8H^+ + 6e^- = 2NH_4^+ \quad E^\ominus = +0.27\ V \quad (18)$$
$$N_2 + 3H_2O = 2NH_3 + 3/2O_2 \quad (19)$$

The maximum energy transition state is located in the first electron transfer (E = −4.16 V) and proton coupled electron transfer (E = −3.20 V) processes, hampering the overall kinetic reaction. It’s worth noting that most photocatalysts cannot produce sufficient electrons to accomplish the reaction due to the fast charge recombination. Fortunately, Z-scheme heterojunctions can efficiently restrain the charge recombination, meanwhile preserve the robust redox capability of the photogenerated holes and electrons, and thus has promising application in N_2 reduction reaction (Eq. 19).

2.2 Photocatalytic performance assessment

Typically, photocatalytic activity can be assessed with the generation rate of photoreaction products. However, the direct

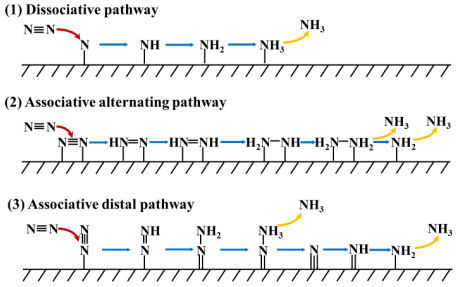

Fig. 2 The traditional mechanisms of N_2 to NH_3.

comparison of photocatalytic activity through product generation rate is not rational due to the variations in practical photoreaction conditions (photocatalyst dosage, light source, lighting area, light intensity and so on) among different laboratories. Therefore, quantum yield is commonly used to assess the photocatalyst's performance at the state-of-the-art of photocatalytic energy conversion. The quantum yield is calculated to the photons' ratio contributing to the photoactivity by the total absorbed photons. Because of light transmission and scattering, it is tough to determining the actual number of photons absorbed by photocatalyst, and thus apparent quantum yield (AQY) is supposed and used with Eq. 20 [18,19,56]:

$$AQY = nR/I \quad (20)$$

where, *n, R*, and *I* refer to the number of electrons (or holes) extracted in the formation of reduced (or oxidized) product molecule, the amount of product molecules produced in a specific time interval, as weel as the incident photon number reaching the photocatalytic system with the interval.

Due to a photocatalyst generally exhibiting different spectral absorption coefficient and photoactivity under different irradiation wavelengths, the AQY value is strongly correlated with the incident light wavelength. It is therefore quite useful to find out the AQY as a function of irradiation wavelength. This AQY assessment method is appropriate for various photocatalytic systems such as water splitting, CO_2 reduction, N_2 fixation, pollutant degradation.

2.2.1 Water photosplitting

The AQY values for water splitting can be calculated using Eq. 20, where, *n, R*, and *I* denote the electron (or hole) number extracted in the formation of single H_2 (or O_2) molecule, the amount of gas molecules produced in a specific time interval, and the incident photon number reaching the photocatalytic system at the same interval. The values of n for HER and OER are 2 and 4 in one-step excitation photocatalytic system, and 4 and 8 in two-step excitation Z-scheme one, respectively. Also, solar to hydrogen (STH) energy conversion efficiency was used to evaluate the performance of water splitting as shown in Eq. 21:

$$STH = (R \times \Delta G_r)/(P_{sun} \times S) \quad (21)$$

where, R, ΔG_r, P_{sun}, and S represent the H_2 generation rate, the Gibbs energy for water splitting reaction, the energy flux of sunlight at the AM1.5 global tilt (100 mW·cm^{-2}), and area of the irradiated photocatalyst, respectively.

The STH energy conversion efficiency is meaningful only if O_2 is generated, that is, overall water splitting reaction occurs. Otherwise, water splitting reaction cannot be used in Eq. 21 with the Gibbs energy. Moreover, the Gibbs energy for water splitting reaction is dependent on the reaction pressure and temperature , and thus the ΔG_r is used in the STH calculation must be adjusted in line with the different conditions. Aslo, the STH is considered as the practical standard for estimating photocatalytic performance with one sun, generally performanced *via* a solar simulator (AM1.5G).

2.2.2 CO_2 photoreduction

In terms of the complex CO_2 photoreduction reactions (usually produces several reductive products), the total consumed electron number (TCEN) per unit time and unit mass of photocatalyst is preferable to estimate the CO_2 photoreduction efficiency. It is calculated by using the product amount and the incident photon number as depicted in Eq. 22:

$$TCEN = [\sum(c_{product} \times n_{electron}) \times V_{reactor}]/(m_{cat.} \times t_{irr.}) \quad (22)$$

where, TCEN is the total consumed electron number for the photocatalytic CO_2 conversion, $c_{product}$ is the concentration of a certain product of CO_2 conversion, $n_{electrons}$ is the consumed electrons per mole of the certain product, $V_{reactor}$ is the reactor volume, $m_{cat.}$ is the photocatalyst mass, and $t_{irr.}$ is the irradiation time. Besides, due to the H_2 is not directly converted from CO_2, it is not considered to calculate the TCEN.

2.2.3 N_2 photofixation

Since the produced NH_3 concentration is usually at low ppm level due to the low efficiency of most photocatalysts, the quantitatively detecting NH_4^+ or NH_3 concentration in solution is fairly challenging. Typically, there are five different assessment methods proposed by ASTM (American Society for Testing Materials) [57,58], US EPA (United States Environmental Protection Agency) [59] and APHA (American Public Health Association) [60]; (i) Ion chromatography (IC); or high performance liquid chromatography (HPLC); (ii) Colorimetric method using Nessler's reagent or phenate; (iii) Ion selective electrode (ISE); (iv) Titration method. The first there methods are extensively applied in experimental research, while the titration method cannot be adopted until the NH_3-N concentration more than 5.0×10^{-6}, and thus is rarely used.

Colorimetric method with Nessler's reagent is a simple and practical method with good reproducibility in laboratory, which makes it the most admissive method in recent investigation. The main shortcoming of colorimetric method is the complex chemical components of products induced by the photocatalytic reactions, which will disturb the assessment. Usually, interference can be caused by urea, hydrazine, glycine, aldehydes, amines and alcohols in different principles [57,61–63]. Also, co-existed cations may influence the results through increasing the turbidity under alkaline conditions. Generally, hole scavengers are widely applied in the N_2 photofixation systems. The oxidation products of hole scavengers and the dissolving ions generated *via* photocatalysts would significantly change the colorimetric reaction of Nessler's reagents [63–65]. Therefore, the colorimetric method using Nessler's reagent usually needs a pre-treatment process. Furthermore, keeping the variables (such as the temperature, humidity and reaction time *etc*.) constant is necessary for obtaining an accuracy and repeatable result [66]. While the impacts imposed by mercury generated from the Nessler's reagents should be attached importance, and thus proper treatment of liquid wastes is of vital importance.

Colorimetric method with phenate is also sdopted to detect the

low concentration of NH_3 in water [67]. The absorbance peak at *ca.* 640 nm is from the indophenol generated by the reaction of NH_3, hypochlorite and phenol under the photocatalysis of sodium nitroprusside. The potential factors affecting the accuracy of measurement. Precipitation by addition of citrate and other ions may increase the turbidity in alkaline solution. In addition, chromatography is more reliable than the other methods because it is based on the analysis with various components which are separated in column before the anaylsis [68,69].

2.3 Characterization technique for Z-scheme mechanism

Generally, the two semiconductors in type II or direct Z-scheme heterostructure have similar band structures. However, the two systems differ in totally reverse electron flow path due to the properties of solid/solid interface. Hence, it is essential to verify the mechanism of Z-scheme's charge transfer employing various characterization methods such as adical trapping experiment, metal cocatalyst loading, sacrificial agent testing, photocatalytic reduction testing and X-ray photoelectron spectroscopy (XPS). Since single characterization method mentioned above is tough to confirm the vectoral charge transfer path in a Z-scheme system, comprehensive characterization and testing should be performed to confirm the electronic structure and charge transfer path.

2.3.1 Metal loading

Photodeposition of noble metal as co-catalyst is one of the classic approaches to confirm the charge transfer path of Z-scheme system. Different from type II heterojunction, a direct Z-scheme system with the interaction at solid/solid interface leads to the redistribution of charge carriers because of the directional electron transfer *via* Ohmic contact from the CB of PS II to the VB of PS I. Consequently, electrons and holes aggregate in PS I and PS II [6], respectively. Under light irradiation and the assistance of corresponding sacrificial agents, the positively charged metal cation will be *in situ* deposited on the electron-rich side (PS I), and hence the accumulation of photogenerated electrons on PS I is testified, indicating the charge transfer path follows a Z-scheme configuration.

2.3.2 Sacrificial reagent testing

Sacrificial reagent can also be utilized to determine the regions of aggregated holes and electrons within a Z-scheme system. In this case, the two-component system should satisfy the following conditions: (1) One semiconductor can only perform the reductive half reaction with sacrificial electron donor; (2) The other can only perform the oxidative half reaction with sacrificial electron acceptors; (3) The two-component system can perform the overall photocatalytic reaction. Zhu *et al.* [70] conducted sacrificial reagent experiment to verify the Z-scheme electron transfer path within black phosphorus (BP)/$BiVO_4$ composite, and found that Co_3O_4-loaded BP and $BiVO_4$ can produce H_2 and O_2 with the help of sacrificial reagent of disodium ethylene diamine tetraacetic acid (EDTA) and $AgNO_3$, respectively. It proves that the PS I and PS II can achieve their reduction and oxidation half reaction, respectively. The Co_3O_4-BP/Co_3O_4-$BiVO_4$ coupled system demonstrated photocatalytic HER under EDTA without O_2 detected and OER under $AgNO_3$ without H_2 production, which testify the photogenerated electron aggregated at BP and $BiVO_4$ was aggregated with photogenerated holes. Moreover, simultaneous H_2 and O_2 evolutions with approximate stoichiometric value were detected when the water photosplitting reaction was measured under pure water with a sacrificial reagent, and therefore sacrificial reagent experiment is feasible to determine the plausible charge transfer mechanism in direct Z-scheme photocatalyst. Nevertheless, this method is only appropriate for the semiconductor with energy band structure solely responsible for the reductive or oxidative reaction of water splitting, while the electron transfer within a bandgap meeting both the reductive and oxidative reactions is not appropriate because it can act as both electron donors and acceptors in the half reaction.

2.3.3 Radical trapping experiment

Radical trapping experiment is another commonly used approach to demonstrate the Z-scheme mechanism. Typically, a chemical reagent is added in the photoreaction system to capture the radical and make the detection easier. Following the heterogeneous photocatalysis's kinetic theory, hydroxide radical (·OH) can be attained by the reaction of OH^-/H_2O with the photoexcited hole of semiconductor with an oxidation potential larger than 2.4 V *vs.* NHE [71]. On the other hand, superoxide radical ($\cdot O_2^-$) is the reduction product from O_2 if the CB of semiconductor possesses sufficient negative potential (less than −0.33 V *vs.* NHE [72]). Therefore, the exploration on the generation efficiency of radicals may illuminate the reaction mechanism on the Z-scheme photocatalyst. Among various radical scavengers, *tert*-butyl alcohol (TBA) and isopropanol (IPA) are the most commonly used ones for scavenging ·OH, while N_2 gas and p-benzoquinone (BQ) are extensively applied for scavenging $\cdot O_2^-$, and TEOA, EDTA and ammonium oxalate (AO) are adopted to scavenge the hole ing [73–76]. To study the underlying charge transfer mechanism of g-C_3N_4/Bi_4O_7, Sun *et al*. [77] found that TBA has slight effect on the degradation of MB (revealing the marginal importance of ·OH), whereas AO and BQ can sharply suppress the degradation activity, demonstrating that $\cdot O_2^-$ and h^+ play an important effect in the photodegradation process.

Electronic paramagnetic resonance (EPR) spectroscopy is also extensively employed to determine the ·OH and $\cdot O_2^-$ in the photoreaction systems for affirming the Z-scheme transfer path [78,79]. Since these radicals cannot be determined directly with EPR, 5,5-dimethyl-1-pyrroline N-oxide (DMPO) is adopted as a trapping reagent for ·OH and $\cdot O_2^-$ to generate DMPO-·OH and DMPO-$\cdot O_2^-$, which can be easily determinate with EPR spectrophotometer. The increasingly higher characteristic peaks of DMPO-·OH and DMPO-$\cdot O_2^-$ with the illumination time prolonging can confirm the generation of ·OH and $\cdot O_2^-$, and then combining the generation potentials of ·OH and $\cdot O_2^-$ (2.4 V and

−0.33 V), the Z-scheme charge transfer mechanism can be assured. For instance, Yang *et al.* [80] reported that a Z-scheme g-C_3N_4/RGO/CoZnAl-LDH with 3D urchin-like structure can efficiently photoconvert CO_2 toward CO, and the Z-scheme charge transfer pathway of CN/RGO/LDH was well confirmed by the EPR spectra through the ·OH and $\cdot O_2^-$ trapping.

2.3.4 *In situ* XPS

As a widely employed determination method of chemical composition and surface state of materials, XPS has been applied to give insights into the charge transfer pathway *via* exploring the relative shift of binding energy of constituent elements [81,82]. A different material introduced on a semiconductor will lead to the binding energy shift of the element in semiconductor if the electron transfer occurs between them under *in situ* light illumination. A positive shift in binding energy demonstrates a decreased of electron density, and the negative shift means an increased electron density, and thus the shift of binding energy in XPS spectra could be applied to confirm the electron transfer pathway of a Z-scheme system. For instance, Low *et al*. [83] identified the Z-scheme charge transfer path in TiO_2/CdS composite employing XPS test. The Ti 2*p* peak gives a slight positive shift and a decrease in the Cd 3*s* peak were observed which can be concluded that the photoexcited electrons transferred from TiO_2 to CdS, which verifies the charge transfer path of the Z-scheme.

2.3.5 Photocatalytic reduction testing

The photoexcited electrons with proper reduction potential in the CB position of the semiconductor can facilitate diverse photocatalytic reduction reactions, and thus it is vital to confirm the accumulation area of those electrons in a specific semiconductor of Z-scheme system by detecting the product of the photoreduction reaction. For example, the CB and VB potential of SnO_{2-x} in SnO_{2-x}/g-C_3N_4 composite is +0.20 V and +2.70 V, the CB and VB potentials of g-C_3N_4 lies at −1.19 V and 1.51 V [84], respectively. If the photocatalytic system obeys the mechanism of type II heterojunction, the redox capability of photogenerated charge carriers will be the minimum. Consequently, the reduction product of CO_2 cannot be detected, because of the CB of SnO_{2-x} (+0.20 V) is more positive than the CO_2 reduction potentials (Eqs. 4–10). However, the redox capability of photogenerated holes and electrons will be the maximum in a Z-scheme photocatalytic system, which allows the recombination of the electrons and holes in the CB of SnO_{2-x} and the VB of g-C_3N_4, and thus the electrons of g-C_3N_4 and holes of SnO_{2-x} can be retained. In the situation, the CB of g-C_3N_4 is enough for CO_2 reduce, and thus confirming the formation of Z-scheme system but not a type II heterostructure.

2.3.6 Other methods

First principle calculation based on the density functional theory (DFT) is a widely used theoretical approach to confirm the experimental results. Especially, theoretical study has been extended to ascertain the charge transfer pathway of the heterostructure and to get an insight into the photocatalytic mechanism [85–95]. For instance, Ma *et al.* [85] investigated the electronic properties and interfacial interaction of g-C_3N_4/WS_2 using DFT calculation to give the mechanism of the charge transfer, and confirmed the existence of built-in electric field from g-C_3N_4 to WS_2 because of the difference. The built-in electric field enhance the electron transfer from WS_2 to g-C_3N_4, and thus a Z-scheme transfer path is used. Similarly, Liu *et al.* [87] investigated the charge distribution, density of states (DOS), and the band offset of the g-C_3N_4/TiO_2 using the hybrid DFT method, and found that the calculated band gap of g-C_3N_4/TiO_2 heterostructure is 1.76 eV. This narrowed band gap contributes to the visible light harvesting. Additionally, the calculated energy indicates that a van der Waals interaction can be formed between the monolayer g-C_3N_4 and the (100) surface of TiO_2, and the g-C_3N_4/TiO_2 heterostructure is a staggered band alignment structure. According to the analysis results of DOS, the built-in electric field's direction (from g-C_3N_4 to TiO_2) and the Z-scheme mechanism of g-C_3N_4/TiO_2 are confirmed.

Besides, effective mass calculation of charge carriers is another method to predict the trend of charge transfer [96–100]. For example, the electronic band structures of PS I and II can be obtained using DFT calculation, and then the effective masses of photogenerated holes and electrons can be calculated by parabolic fitting to the valence band maximum (VBM) and conduction band minimum (CBM) using the Eq. 23, respectively. According to Eq. 24, where v and m^* denote the effective mass and transfer rate of a charge carrier, it can be concluded that the effective mass of charge carrier is inversely proportional to the moving velocity. That is, the charge carrier with less effective mass would give the fast transfer [96–100].

$$m^* = \hbar^2(\mathrm{d}^2E/\mathrm{d}k^2)^{-1} \quad (23)$$

$$v = \hbar k/m^* \quad (24)$$

In addition, Z-scheme charge transfer path can be measured by surface potentials of semiconductors through surface photovoltage spectroscopy (SPS), Kelvin probe force microscopy (KPFM) and transient absorption spectroscopy (TAS) [101,102]. The development of the characterization techniques to determine Z-scheme systems promotes the understanding of charge transfer and separation pathways during the photocatalytic process, and gives deeper insights into further optimization of the capability of photocatalytic systems. The next sections will focus on the development and energy conversion applications of Z-scheme heterostructures as well as the strategies to improve photocatalytic performance.

3 Energy conversion application of Z-scheme photocatalyst

The weak light absorption and low efficiency under solar light illumination always persist. Compared with the standard type II heterojunction and the single-component semiconductor, construction of Z-scheme heterojunction can broaden the spectral response range, suppress the charge recombination and preserve the strongest redox capacity of photogenerated holes

and electrons, thus sharply elevated the photocatalytic performance [103]. So far, numerous semiconductors including inorganic, organic and inorganic-organic hybrid materials have been successfully developed to the fabrication of Z-scheme heterostructures. The large amounts of semiconductors and increasingly improved photocatalytic performance suggested the fascinating application prospect of energy conversion *via* Z-scheme mechanism. The following sections will focus on the applications of various Z-scheme heterojunctions (inorganic [6,70,83,104–151], organic [125,152–154], and inorganic-organic hybrid [80,155–200] materials) in the studies of energy conversion.

3.1 Inorganic Z-scheme photocatalyst

Some metal oxides with d^0 electronic configuration cations (*i.e.*, Ti^{4+}, Zr^{4+}, Ce^{4+}, Ta^{5+}, Nb^{5+}, W^{6+} *etc.*) or d^{10} electronic configuration ones (*i.e.* Zn^{2+}, In^{3+}, Ga^{3+}, Sn^{4+}, Ge^{4+}, Sb^{5+}, Mo^{6+}, *etc.*) are usually wide bandgap semiconductors and commonly used as photocatalyst for UV light absorption [103]. Among which, TiO_2 is the most exploited photocatalyst featuring with long-term stability, nontoxicity and low-cost properties [201]. However, TiO_2 can only absorb UV light because of the fast charge recombination and large bandgap energy ($E_g \approx 3.2$ eV), while UV light only occupies less than 5% of solar spectrum [19]. Therefore, various inorganic narrow bandgap semiconductors (such as CdS, NiS, WO_3, Fe_2O_3, $BiVO_4$ and even black phosphorus) were developed to combine with wide bandgap semiconductors (TiO_2, ZnO, SnO_2 *etc*.) for a satisfactory photocatalytic performance.

3.1.1 Water photosplitting

It is still a challenging to achieve overall water splitting to simultaneously produce H_2 and O_2 without the utilization of sacrificial reagent. Compared with the two-electron HER, the OER involves in $4e^-$ and $4H^+$ along with the formation of O—O bond, which has a large overpotential because of the high kinetic barrier [202]. Therefore, water oxidation has been considered as the water splitting's rate-determining step, and thus is more challenging [203]. Generally, some metal oxides, such as WO_3, Fe_2O_3, $BiVO_4$ *etc.*, have continuous and wide absorption spectrum as well as good stability in water, but the low charge separation causes low OER activity [204], therefore combining them with narrow bandgap reductive semiconductor to construct heterojunctions is an alternative strategy to realize overall water splitting. Among which, a preferable method is to construct Z-scheme heterojunctions. Under light illumination, both of the two semiconductors are excited, one of them is utilized to reduce water to H_2, and the other oxidizes water to O_2. The photogenerated electrons of reductive semiconductor can give the holes recombing in the oxidative aspect, and thus the bandgap of the single material does not need to straddle both the HER and OER potentials [104–127,142–145].

Wang *et al.* [124] designed photocatalyst based on La- and Rh-codoped $SrTiO_3$ ($SrTiO_3$:La,Rh) as H_2 evolution photocatalyst (HEP) and $BiVO_4$ with Mo-doped ($BiVO_4$:Mo) as O_2 evolution photocatalyst (OEP) embedded into an Au layer, which was studied by the energy dispersive X-ray (EDX) mappings and top-view of the scanning electron microscope (SEM) image. After depositing Ru species on $SrTiO_3$:La,Rh and $BiVO_4$:Mo particles as cocatalysts, the resultant Ru-modified $SrTiO_3$:La,Rh/Au/$BiVO_4$:Mo exhibited Z-scheme mechanism and overall water splitting activity with a record STH of 1.1% and an AQY of 33% at 419 nm. Since Cr_2O_3 shell capping noble metal nanoparticles can suppress the backward reactions whilst maintaining the function of the noble metal as HER catalyst [205,206], Cr_2O_3 was deposited on the $SrTiO_3$:La,Rh/Au/$BiVO_4$:Mo which have been modified by Ru. The photocatalyst sheet exhibited an excellent activity for the water splitting without any supporting electrolyte or buffering reagent. Given the low cost and high STH, the photocatalyst sheet may boost the advances of industrial solar-driven hydrogen production [124].

Zhu *et al.* [70] give an artificial Z-scheme system constructed by two-dimensional (2D) heterostructure of black phosphorus (BP)/$BiVO_4$. Since BP nanoflake is an good visible and near-infrared (NIR) light-driven photocatalyst for HER [207,208], and $BiVO_4$ with suitable band position is preferable to OER [209], the resultant BP/$BiVO_4$ delivered overall water splitting performance with optimum HER and OER rates of *ca.* 160 and 102 $\mu mol \cdot g^{-1} \cdot h^{-1}$ under visible light ($\lambda > 420$ nm) irradiation without sacrificial reagent or external bias. After modified by Co_3O_4, an improvment of nearly 5 times was achieved for H_2 and O_2 production, respectively. Meanwhile, the kinetic mechanism of photoexcited state was analyzed using femtosecond time-resolved diffuse reflectance (TDR) spectroscopy [70]. Liu *et al.* [118] reported a black/red phosphorus (BP/RP) heterophase junction, which was *in situ* constructed with bulk RP as a feedstock and ethylenediamine as solvent. Raman spectra (Fig. 3a) and TEM image (Fig. 3b) prove that they are with high-quality interfacial contact and crystallized BP are interlaced with amorphous RP. This structure feature provides the foundation of Z-scheme charge transfer pathway (Fig. 3c,d) for water splitting without sacrificial reagent under visible light illumination [118]. To clarify the efficient interfacial charge transfer *via* a direct Z-scheme pathway, the real-time carrier dynamics were tried to tracked by the time-resolved transient absorption spectra (TAS) under 400 nm excitation (Fig. 3e–h) [210–213]. According to the variation of absorption bands and the decay kinetics parameters (lifetime) of the TAS spectra, the Z-scheme mechanism was unambiguously confirmed [118].

Of course, H_2 can also be obtained through the reduction half reaction of water photosplitting by the assistance of sacrificial reagent. Typically, CH_3OH, C_2H_5OH, AA, EDTA and TEOA are the popular sacrificial electron donor (or hole scavenger) in the photocatalytic HER process. Xu *et al.* [104] fabricated TiO_2/NiS core-shell photocatalyst for HER. The EDX mappings (Fig. 4a) indicated the successful fabrication of TiO_2/NiS composite. TN10 presented the superior performance of 655 $\mu mol \cdot h^{-1} \cdot g^{-1}$

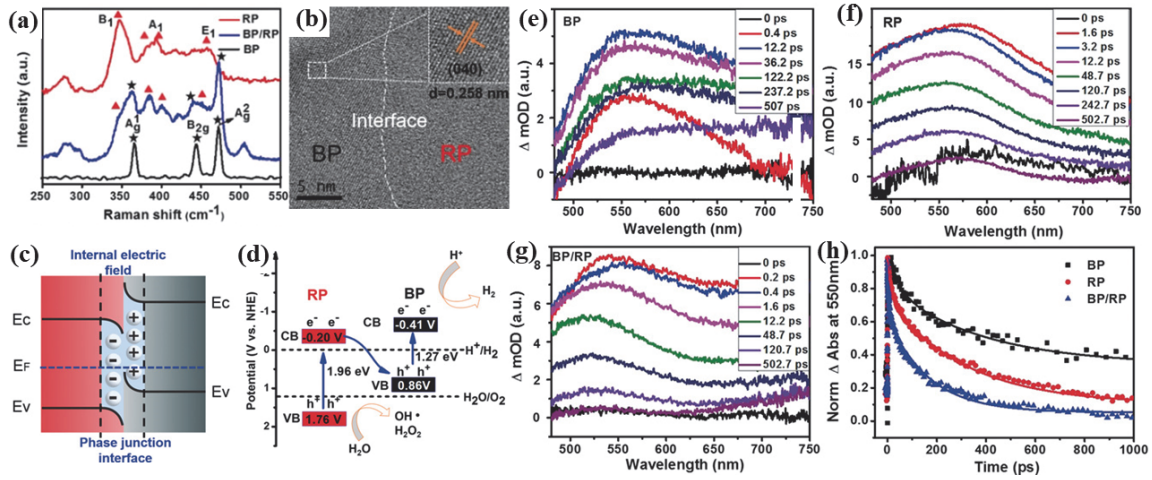

Fig. 3 Raman spectra (a) and HRTEM image (b) of the BP/RP heterophase junction. (c) The energy band and interface charge property. (d) Scheme of direct Z-scheme charge transfer. TAS of BP (e), RP (f) and BP/RP (g) after irradiation. (h) Normalized TAS at 550 nm.

Adapted and reproduced with permission [118]. Copyright 2019, Wiley.

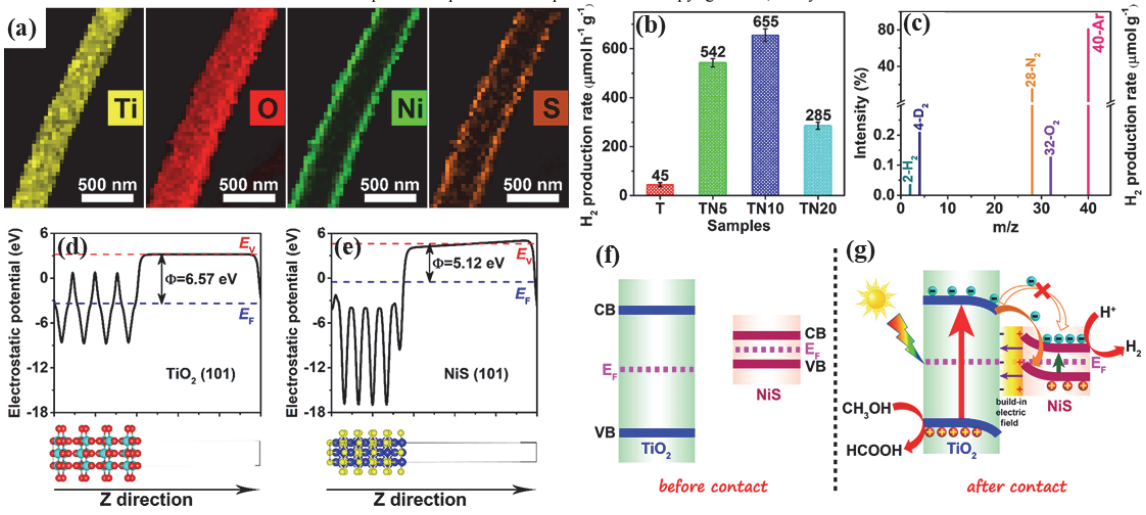

Fig. 4 (a) EDX of Ti, O, Ni and S in TN10. (b) Comparison of photocatalytic HER activities. (c) GC-MS spectra obtained after injecting 0.5 mL samples of the gas produced by D_2O splitting under UV-Vis light for 2 h. (d) Calculated electrostatic potentials for (101) facets of TiO_2 and NiS. (e) Scheme of direct Z-scheme heterojunction before (f) and after (g) contact along with the charge transfer and separation under UV-Vis light.

Adapted and reproduced with permission [104]. Copyright 2018. The American Chemical Society.

under UV-Vis light by using CH_3OH (Fig. 4b). Isotopic tracer experiment indicated that both D_2 and H_2 were detected in the product (Fig. 4c), demonstrating that D_2 was originated from water splitting. Due to the proton exchange between D_2O and H_2O, a trace of H_2 coexisted [104]. Furthermore, *in situ* XPS spectra indicated that the binding energy of Ti 2*p* and TN10' O 1*s* under irradiation exhibited a positive shift of *ca.* 0.4 eV compared with those in dark, and those of Ni 2*p* and S 2*p* shifted by 0.5 eV toward a lower value under light. These binding energy shifts show that the photoinduced electrons in the CB of TiO_2 can migrate to NiS under UV-Vis, which further proves the proposed direct Z-scheme charge transfer pathway. Noticeably, DFT calculation also shows that the work functions of TiO_2 is 6.57 eV and NiS is 5.12 eV (Fig. 4d,e), respectively. It demonstrates that the NiS's Fermi level is higher than TiO_2, causing the electron transfer from NiS to TiO_2 upon contact until their Fermi levels are aligned. This electron transfer generates an internal electric field pointing from NiS to TiO_2 at TiO_2/NiS interface (Fig. 4f,g), which is agreement with the *in situ* XPS analysis [104]. The wisely characterization method combining experimental analysis with theoretical calculation provides new idea for insight into the other efficient Z-scheme photocatalysts.

Liu *et al.* [214] utilized metal organic framework (MOF) as guiding reagent for fabricating inorganic Z-scheme photocatalyst, which is composed by small-sized Co_9S_8/CdS heterostructure, derived from the sulfidation of Cd/Co-MOF solid solution, and an excellent HER activity of 61.924 mmol·g^{-1} in 6 h with good selectivity for benzyl-alcohol (BA) oxidation, nearly 21 times than that of the single CdS and 16 times than the physical mixture with Co_9S_8. The uniformly distributed with each other to form Co_9S_8/CdS Z-scheme heterostructure because of the binding abilities are different between Co-S and Cd-S. The time-resolved and steady-state photoluminescence (PL) spectra demonstrated that the pure CdS's charge carrier lifetime is 1.54

ns which is largely shortened to 1.10 ns in the heterostructure. Also, the steady-state PL spectra exhibit that the peak intensity of CdS is totally quenched by Co_9S_8 at *ca.* 500 nm [214]. These study indicate that additional electronic transfer channels is exis from CdS to Co_9S_8, demonstrating that the photoexcited charge recombination in CdS is effectively retarded. The novel preparation method with MOF serving as guiding reagent opens a new avenue for fabricating efficient inorganic Z-scheme photocatalysts.

3.1.2 CO_2 photoreduction

During the photocatalytic conversion of CO_2 into hydrocarbons, CO_2 reduction half reaction and H_2O (or sacrificial reagent) oxidation half reaction are two basic factors to affect the photocatalytic energy conversion efficiency. Both of them are multi-charge transfer processes, which require simultaneous accumulation of multiple holes and electrons at two different active sites [215,216]. Furthermore, the two half reactions are coupled and interacted [217]. The required fast migration of the photogenerated holes and electrons for high reaction performance are hard to be achieved with a single-component photocatalyst. Therefore, various inorganic Z-scheme heterojunctions has been designed and fabricated for overcoming the above problems [128–138,144].

Li *et al*. [133] has utilized two narrow bandgap inorganic semiconductors to fabricate an all-solid-state Z-scheme heterojunction (WO_3/Au/In_2S_3, Fig. 5a), which presented CH_4 with 0.42 μmol·g^{-1}·h^{-1}, higher than the counterparts (Fig. 5b). The enhanced photoactivity was attributed to the efficient Z-scheme charge transfer pathway and the ultrathin In_2S_3 nanosheets (~5 nm) that shortens the diffusion distance of photogenerated electrons and holes to the semiconductor surface. The Z-scheme charge transfer pathway was studied by

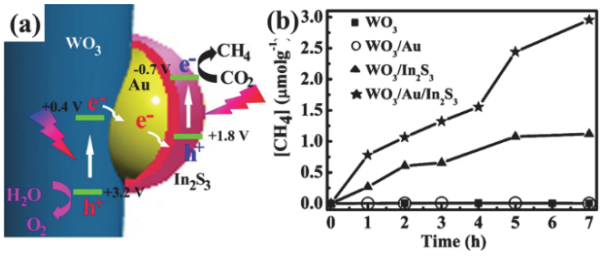

Fig. 5 (a) CH_4 yield during a period of irradiation. (b) Z-scheme charge transfer in WO_3/Au/In_2S_3.

Adapted and reproduced with permission [133]. Copyright 2016, The American Chemical Society.

measuring the surface potentials of WO_3/Au/In_2S_3 and other WO_3-based counterparts using the probe force microscopy (KPFM) technique. The result showed that the holes tended to aggregates on WO_3 surface, manifesting the directional transport of electrons occupying the CB of WO_3 through Au to the VB of In_2S_3, and recombining with the holes on the VB of In_2S_3 (Fig. 5a), which obeyed the Z-scheme charge transfer mechanism [133]. It implies that the skillfully utilization of advanced technologies can obtain the information of the surface states, which is giving deep insight into the charge transfer in the heterojunction.

Also, direct Z-scheme heterojunctions were fabricated to achieve high-efficiency CO_2 reduction. Low *et al*. [83] fabricated the TiO_2/CdS composite delivered a CH_4 activity of 11.9 mmol·h^{-1}·m^{-2} under simulated sunlight, higher than that of the single CdS or TiO_2. Notably, the charge transfer mechanism was confirmed through an *in situ* irradiated X-ray photoelectron spectroscopy (ISI-XPS). Recently, Wang *et al*. [131] reported a kind of 3D-SiC@2D-MoS_2 nanoflower-like composite with a unique Z-scheme energy band (Fig. 6a,b), which achieved the overall conversion of CO_2 under visible light. The corresponding CH_4

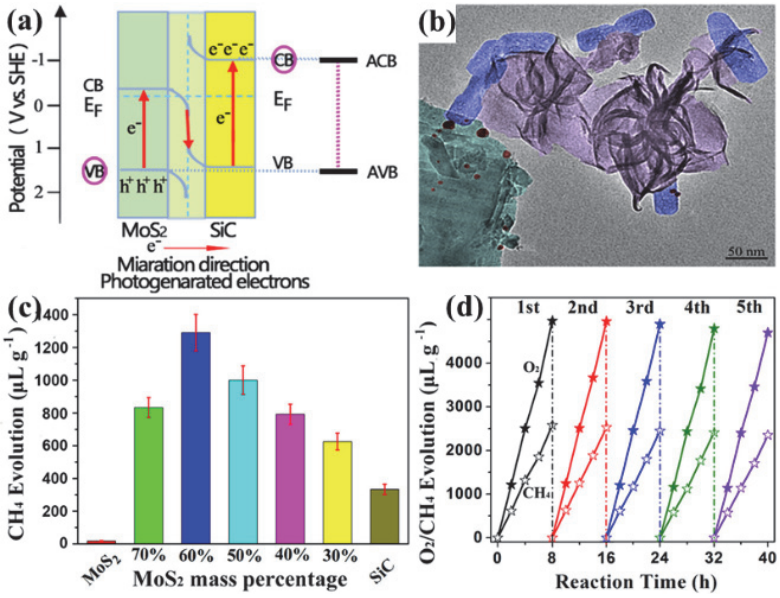

Fig. 6 (a) Z-scheme model of SiC@MoS_2. (b) TEM image of the SiC@MoS_2. (c) CH_4 evolution on the SiC@MoS_2 with different MoS_2 contents for 4 h, (d) Stability of SiC@MoS_2-60% during five cycles.

Adapted and reproduced with permission [131]. Copyright 2018, The American Chemical Society.

production activity is 323 $\mu L \cdot g^{-1} \cdot h^{-1}$ along with stoichiometric O_2 evolution activity (Fig. 6c,d), which is a record for simultaneously CO_2 reduction to CH_4 together with H_2O oxidation under visible light illumination. The superior photocatalytic performance was attributed to the factors [131]: (i) The heterostructure of direct Z-scheme; (ii) The higher electron and hole mobility of the components; (iii) The specific 1D heterojunction formed by 2D-MoS_2 fixing on the 3D-SiC surface, and the morphology of SiC@MoS_2 make the surface exposed and accessible to reactants; (iv) The reaction operated in the gas-solid reaction. In addition, the control experiment with $^{12}CO_2$ or $^{13}CO_2$ as the reactant verified that CH_4 is stemmed from the CO_2 photoreduction, and the experiment using $H_2{}^{18}O$ suggested that O_2 is derived from the reduction reactions of both the added $H_2{}^{18}O$ and $C^{16}O_2$ [131].

3.1.3 N_2 photofixation

Photocatalytic N_2 fixation is an interesting NH_3 production method alternative to the Haber-Bosch reaction. In this process, the photoinduced holes and electrons of semiconductor move to the CB and VB, respectively. The holes in VB oxidize H_2O to O_2, together with the CB's electrons reduce N_2 to NH_3, but the low quantum yield is always suffered in N_2 photofixation due to the fast charge recombination and the robust triple bond of N_2 (bond energy: 941 $kJ \cdot mol^{-1}$). Construction Z-scheme heterojunction is a preferable way to retarding the charge recombination, and boosting the N_2 fixation performance.

Rong *et al.* [139] reported $TiO_2/ZnFe_2O_4$ Z-scheme photocatalytic system toward the synthetic NH_3 by N_2 fixation, and the NH_3 by ZFO($ZnFe_2O_4$) and MT (modified TiO_2)/ZFO increases with the time of irradiation, while no NH_3 was detected for the pure MT. The pure $ZnFe_2O_4$ possesses visible-light-responsive feature, but the high charge recombination leads to a relatively low activity. The NH_3 generation rate over the MT/ZFO arrived about 1.48 $\mu mol \cdot L^{-1} \cdot min^{-1}$, which could keep over 600 min, demonstrating a good photostability. The photoexcited electrons in the ZFO's CB transferred to the MT's CB, and the photoinduced holes in the MT'VB transferred to the ZFO'VB. In this way, the ZFO's VB potential is 0.38 eV, a little positive than the potentials of $OH^-/\cdot OH$ (1.99 eV *vs*. NHE) and H_2O/H^+ (1.23 eV *vs*. NHE) thus the active species of ·OH and H^+ could not be generated. Fortunately, a direct Z-scheme was formed since it was found that the photoinduced electron transferred from the MT'CB and recombine with the holes in the VB of ZFO, and then more negative reduction potential in the CB of ZFO and positive oxidation potential in the VB of MT were preserved, resulting in a better redox ability. This work may inspire the development of inorganic semiconductors in N_2 photofixation.

3.2 Organic Z-scheme photocatalyst

Organic polymer semiconductors including conjugated microporous polymers (CMP), covalent organic frameworks (COFs) and even MOFs are usually based on earth-abundant elements and have advantages over the inorganic photocatalysts due to the well-arranged structure and accessible pores together with the tunable opticale and lectrical features, which can be easily attained through molecular engineering. Therefore, organic semiconducting materials have become the promising candidates for photocatalytic energy conversion. Currently, the highest reported STH efficiency (1.1%) was achieved in an inorganic semiconductor Z-scheme system [119]. In principle, the similar approach can also be applied to organic polymer photocatalysts by combining organic polymer semiconductor with another organic one to form Z-scheme heterojunction, where the photogenerated holes and electrons are separated on the divided sub-systems, thereby retarding the charge recombination and allowing for longer lifetime of charge carriers to overcome the kinetic limitations.

3.2.1 Water photosplitting

Due to the high surface area and predictability to assemble diverse molecules with controllable electronic properties, organic polymer semiconductors have also been applied to water splitting [125,218–220]. While the complicated fabrication processes and usually poor long-term stability confine the wide-spread utilization of organic polymer semiconductors. In 2018, a pure organic polymer-based 2D/2D heterojunction was fabricated using aza-fused CMPs and C_2N polymer nanosheets (Fig. 7a,b) with a direct Z-scheme mechanism (Fig. 7c) [125], and the resultant 2D/2D polymer heterojunction with an optimum mass ratio presented efficient and stable overall water splitting activity with a $H_2 : O_2 = 2 : 1$ (Fig. 7d,e), while only aza-CMP or C_2N component is inactive. X-ray absorption near-edge structure (XANES) spectroscopy, EDX element mappings and high-angle annular dark-field scanning transmission electron microscopy (HAADF-STEM) image were applied to study the interactions and combination of aza-CMP and C_2N nanosheets. The STH value of 0.23% for overall water splitting can increase to 0.40% by using reduced graphene oxide (RGO) as solid electron mediator. This result is originating from the properly aligned band structures, reduced charge diffusion distance, efficient charge transfer and separation. The application of 2D/2D polymer heterojunction in Z-scheme provide a guidance for designing novel organic polymer photocatalysts from the view of the component and morphology.

Wan *et al.* [218] designed twelve 2D nitrogen-linked COFs based on the first-principle calculations (Fig. 8a–c). Among which, the COFs built with three N-containing linkages are capable of water splitting because their CBM and VBM positions are suitable (Fig. 8d). The band alignment of a Z-scheme built with 2D Ao-TA and aza-CMP (Fig. 8e) and the free energy change is negative when considering the light-induced electrons (U = 1.05 eV, Fig. 8f). Moreover, the Ao-TST@CMP would have an absorption edge of *ca.* 650 nm (Fig. 8g) as calculated from the bandgap of 2D Ao-TST. This work presents a pass to design practical 2D COFs as single-material and metal-free photocatalyst.

Liu *et al.* [219] reported a sandwich structured Z-scheme photocatalyst of polyaniline (PANI)-Ag-CN, which the Ag

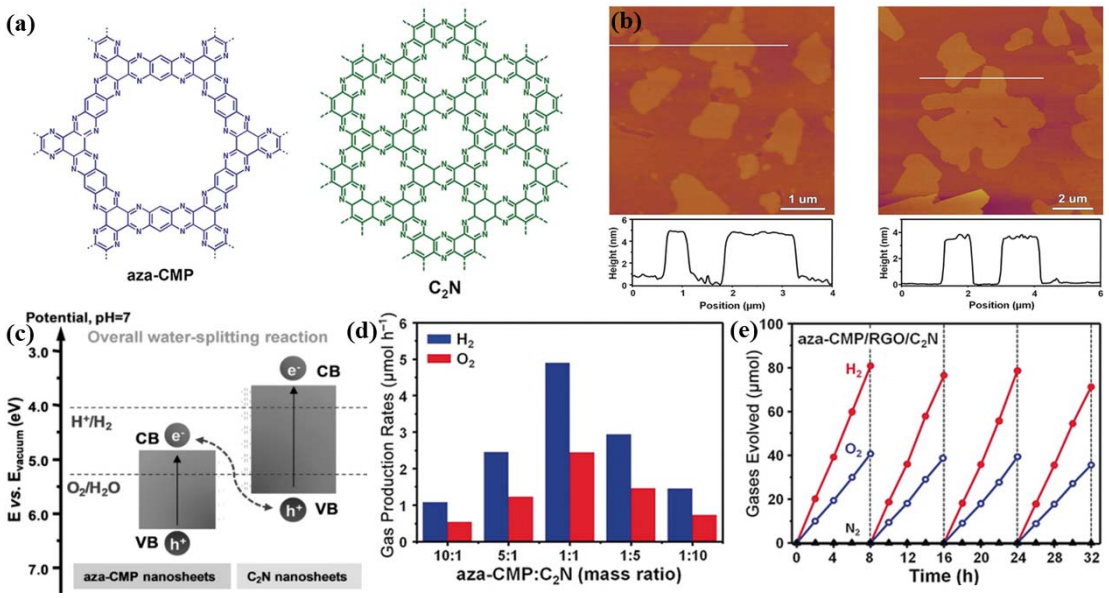

Fig. 7 (a) Chemical structures of aza-CMP and C_2N. (b) AFM and the height profiles of aza-CMP (left) and C_2N (right). (c) Illustration of the electronic band structures. (d) The overall water splitting performance of aza-CMP/C_2N. (e) Typical time course of H_2 and O_2 over aza-CMP/RGO/C_2N.

Adapted and reproduced with permission [125]. Copyright 2018, Wiley.

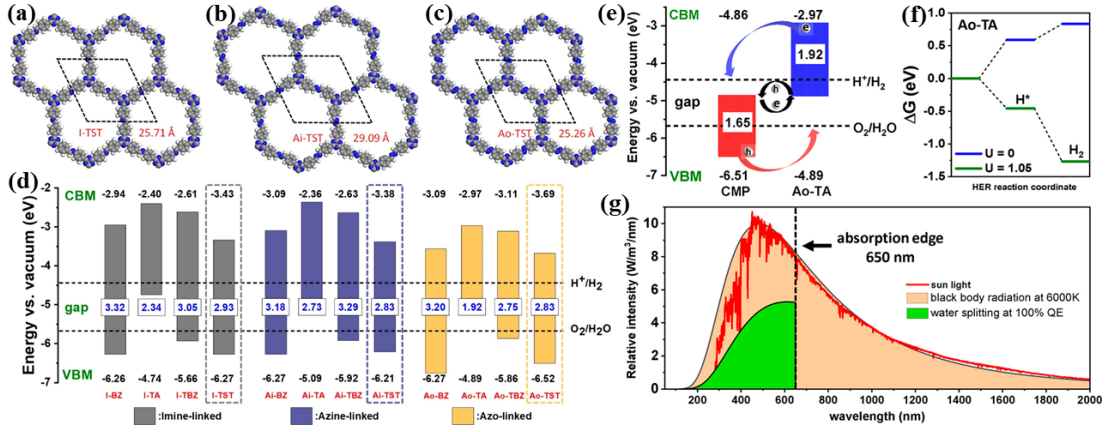

Fig. 8 (a–c) structures of I-TST, (a) Ai-TST (b) Ao-TST (c) COFs. (d) The calculated energy positions of VBM and CBM of 2D COFs. (e) Band alignment of aza-CMP and Ao-TST. (f) Gibbs free energy change for HER. (g) Estimated solar-to-energy conversion efficiency.

Adapted and reproduced with permission [218]. Copyright 2020, The American Chemical Society.

nanoparticles are loaded as the charge transfer intermediate. g-C_3N_4 nanosheets were fabricated through the proton acidification thermal polymerization method, and Ag nanoparticles were then deposited on the g-C_3N_4 surface using chemical reduction process. By combining PANI and Ag-CN *via* stripping, the Z-scheme sandwich photocatalyst was attained. Although the HER activity of those bulk photocatalysts was lower, the short charge transfer path and large number of active sites on the ultrathin nanosheets are good to the photocatalytic HER, and the PANI-Ag-CN exhibits an enhancement of 5048 $\mu mol \cdot g^{-1} \cdot h^{-1}$, 43.52- and 58.02-fold of g-C_3N_4 nanosheets and bulk g-C_3N_4, respectively. In 2018, Zhou *et al*. [220] combined the NH_2-MIL-125(Ti) MOFs with g-C_3N_4 functionalized by benzoic acid (CFB) to synthesize a novel CFB/NH_2-MIL-125(Ti) composite (named as CFBM). The benzoic acid in CFBM acts as electron mediator to achieve rapid charge separation. The experimental results show that the NH_2-MIL-125(Ti) and g-C_3N_4 delivered low H_2 production rate, while the CFB delivers a higher rate than the g-C_3N_4. It indicates that the carboxylic groups on CFB surface can boost the activity of g-C_3N_4. And the H_2 production rate of CFB/MOFs with 10% (*w*) CFB (10CFBM) is 1.123 $mmol \cdot h^{-1} \cdot g^{-1}$ with a robust stability. According to the comprehensive characterizations, the possible formation process of CFBM and its Z-scheme mechanism were proposed. This work gives a good example to get a metal-free semiconductor/MOFs connected by covalent bonds.

Unfortunately, organic polymer semiconductors capable of CO_2 reduction and N_2 fixation in Z-scheme reaction path are rare right now, partly due to the severe charge recombination and the rigorous requirements to the band alignments. On the other hand,

the oxidative potentials and reductive potentials of CO_2 reduction and N_2 fixation are higher than water splitting. Therefore, novel polymers possessing high performance are highly desired for CO_2 reduction and N_2 fixation.

3.3 Inorganic-organic hybrid Z-scheme photocatalyst

A number of metal-free organic semiconductors possessing earth cost-effective, abundance, easy fabrication and good mechanical flexibility merits have been developed. For instance, g-C_3N_4, which consists of triazine (C_3N_4) and tri-s-triazine/heptazine (C_6N_7) rings, has been extensively used in photocatalytic water splitting and CO_2 reduction owing to its earth-abundant feature, facile fabrication circuit, appealing bandgap energy and high physicochemical stability. Meanwhile, porphyrin and phthalocyanine are attracting organic dye thanks to their intense visible light absorption, and the substitutions of the conjugate ring can moderate the electrochemicalp and hysicochemical properties. The movements can also construct the oriented electron transfer pathways [221–223]. In addition, the central metal ions can enhance the stability of porphyrin and phthalocyanine as well as some other fascinating properties, and thus the derivatives of metalloporphyrins and metal phthalocyanines have been widely used in artificial photosynthetic systems for energy conversion [155,224].

Besides, COFs and MOFs, as highly crystalline porous polymers, has ordered structure, high surface area, well-accessible pore walls, tunable optical and electrical properties [225,226]. All these features make MOFs and COFs to be promising candidates for photocatalytic reactions. Similarly, CMPs would also be promising photocatalysts due to the high porosity combining with excellent solution dispersion, which can promote the uniform contact of heterogeneous materials with contaminants to improve the photoactivity. Also, CMPs can further combine different electron donor/acceptor groups and change the nanostructure to promote the charge transfer and enhance the redox sites for improving the photocatalytic performance. However, those organic semiconductors usually exhibit severe charge recombination, and thus are combined with other inorganic semiconductors to form inorganic-organic hybrids for boosting the photocatalytic performance [227–260].

3.3.1 Water photosplitting

The construction of a Z-scheme heterostructures using inorganic-organic hybrid materials is an effective approach to promote the separation and transfer of photoexcited charge and the HER activity. Especially, the inorganic-organic hybrid Z-scheme systems can take full advantages of easy fabrication and appealing bandgap energy (inorganic materials) and finely moderated physicochemical and electrochemical properties, highly porous merits (organic materials), and therefore many systems have been successfully utilized in water splitting [188–192,199]. More recently, Zhang *et al.* [227] used COF, TpPa-2-COF to integrate with a-Fe_2O_3 for constructing Z-scheme inorganic-organic hybrids. The optimal a-Fe_2O_3/TpPa-2-COF heterojunction shows a HER rate of 3.77 mmol·h^{-1}·g^{-1} without co-catalyst under visible light illumination. The PL, TRPL, EIS and EPR measurements were conducted to confirm the Z-scheme charge transfer mechanism. This is a novle COF-based Z-scheme photocatalyst without noble metal, and opens a novel way for the design of COF-based photocatalysts.

To attain a satisfactory STH conversion efficiency, wide spectral responson and highly efficient charge generation are the two essential requirements for a photocatalyst. The blue $W_{18}O_{49}$ with E_g = 3.0 eV displays an intense localized surface plasmon resonance (LSPR) absorption in Vis-NIR owing to the abundant surface oxygen vacancies [156,157,228–231]. While the LSPR-excited "hot electrons" on $W_{18}O_{49}$ are inactive for HER in the absence of an active medium. Combining the plasmonic $W_{18}O_{49}$ for fabricating a Z-scheme heterostructure is a desired strategy to surmount the issue and successfully achieve the wide spectrum responsive (UV-Vis-NIR) HER. The CB potential of g-C_3N_4 has sufficient capacity to reduce H^+ and its VB potential is slightly more positive than the CB potential of common tungsten oxide [158–160]. Therefore, 2D g-C_3N_4 is a preferable choice for coupling with plasmonic $W_{18}O_{49}$ to form a Z-scheme photocatalyst.

A interesting nonmetal plasmonic Z-scheme photocatalyst with $W_{18}O_{49}$/g-C_3N_4 heterostructure is reported by Zhang *et al*., which can effectively capture sun light from UV to NIR region and simultaneously possesses improved charge transfer dynamics to promote the generation of long-lived active electrons for HER (Fig. 9a) [161]. The $W_{18}O_{49}$/g-C_3N_4 heterostructure exhibited a 3.2-fold boost on H_2 rate compared to the single g-C_3N_4 (Fig. 9b–d), which can be ascribed to the effect between the semiconducting Z-scheme charge separation and metal-like LSPR-induced "hot electrons" injection process. Appropriate energy bands alignment between $W_{18}O_{49}$ and g-C_3N_4 endow their combination to present a Z-scheme charge transfer process, as evidenced by the steady-state PL spectra and the time-resolved PL decay (TRPL) analysis. After combining $W_{18}O_{49}$ nanograsses to form the heterostructure, there is a obviously quenched of g-C_3N_4 nanosheets (≈ 430 nm) (Fig. 9e), indicating either the shorter lifetime of the photoexcited electrons with the faster migration process or the longer lifetime of the electrons with the slower recombination. According to the TRPL curve of the $W_{18}O_{49}$/g-C_3N_4 and the single g-C_3N_4 nanosheets (Fig. 9f), the τ_1 (1.9 ns) and τ_2 (8.5 ns) for $W_{18}O_{49}$/g-C_3N_4 are longer than that of the single g-C_3N_4 nanosheets (τ_1 = 1.9 ns; τ_2 = 8.5 ns). This enhanced fluorescent lifetime further demonstrates the retarded radiative recombination with the long-lived photoexcited electrons on the photoexcited g-C_3N_4 nanosheets owing to the coexisted $W_{18}O_{49}$ nanograsses since it can trap the photoexcited holes on the VB of g-C_3N_4 nanosheets to form the corresponding hole vacancies. Besides, the band theory analysis was utilized to analyze the LSPR. As shown in Fig. 9g, the threshold wavelength for exciting the LSPR driven HER is around 900 nm for $W_{18}O_{49}$/g-C_3N_4, shows the possiblity

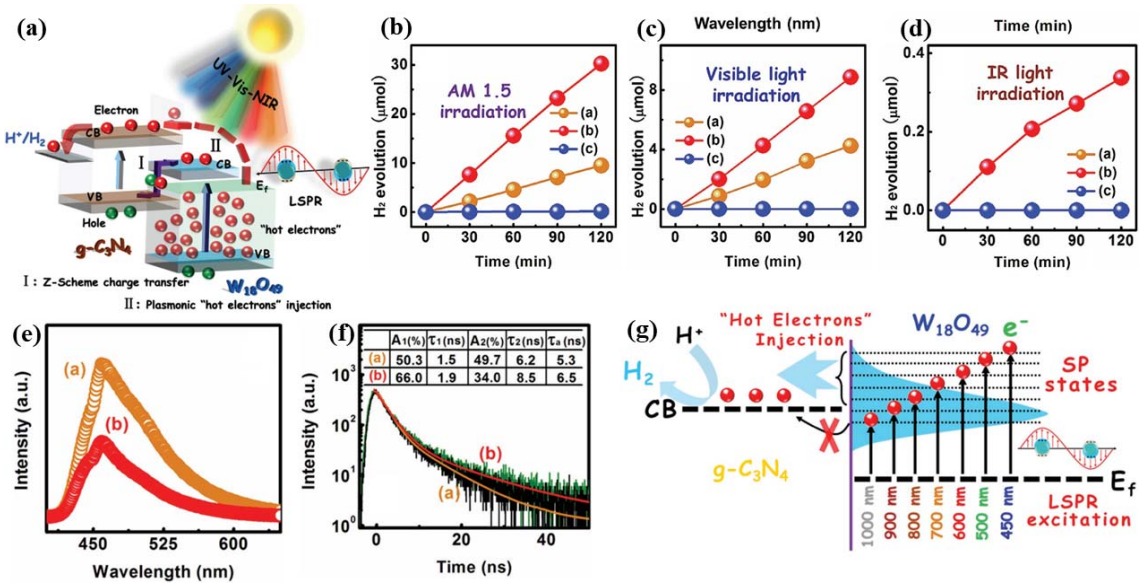

Fig. 9 (a) Charge generation/transfer process in $W_{18}O_{49}$/g-C_3N_4 heterostructure. (b–d) The photocatalytic performance under simulated sunlight (b), visible light (c) and IR light (d) irradiation (in which (a) g-C_3N_4 nanosheets, (b) $W_{18}O_{49}$/g-C_3N_4 heterostructure, and (c) $W_{18}O_{49}$ nanograsses). (e, f) Steady-state PL spectra (e) and TRPL decay curves (f) (in which (a) g-C_3N_4 nanosheets and (b) g-C_3N_4/$W_{18}O_{49}$ heterostructure). (g) Schematic diagram of plasmonic "hot electrons" injection process from $W_{18}O_{49}$ to g-C_3N_4.

Adapted and reproduced with permission [161]. Copyright 2017, Wiley.

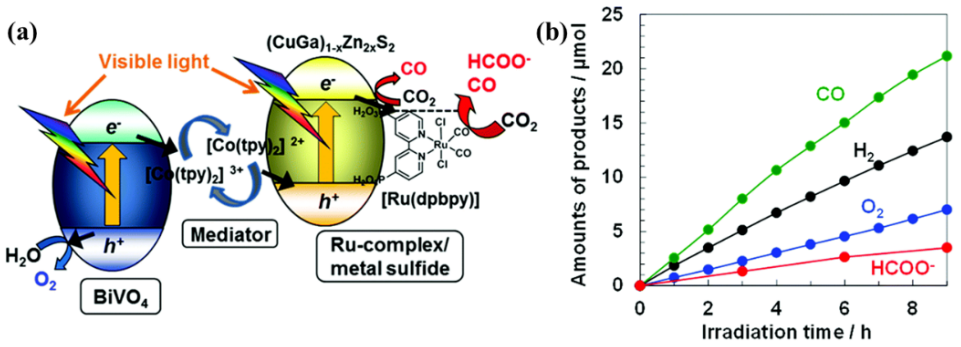

Fig. 10 (a) The construction of $BiVO_4$ catalyst, [Ru(dpbpy)] modified $(CuGa)_{1-x}Zn_{2x}S_2$, and a $[Co(tpy)_2]^{3+/2+}$ redox. (b) Z-schematic CO_2 reduction rate.

Adapted and reproduced with permission [174]. Copyright 2018, The Royal Society of Chemistry.

for this nonmetal LSPR-induced HER process in the viewpoint of band theory.

3.3.2 CO_2 photoreduction

Typically, combining metal complexes with inorganic semiconductor to form hybrid photocatalyst will drastically promote the selectivity of CO_2 reduction due to the selective coordination of CO_2 to the complex's metal centers [172], and thus construction inorganic-organic hybrid heterojunction is a fascinating method to elevate the CO_2 reduction performance [174–176,180–187,232–237].

Suzuki *et al.* creatively fabricated the [Ru(dpbpy)]-modified $(CuGa)_{1-x}Zn_{2x}S_2$ with $BiVO_4$ to form a Z-scheme photocatalyst for CO_2 reduction, assisted by the redox couple of $[Co(tpy)_2]^{2+/3+}$ (Fig. 10a) [174]. In the long-term stability reaction, the optimized Z-scheme photocatalyst (x = 0.7) presented turnover numbers (TONs) of 214 and 70 for CO and $HCOO^-$ (Fig. 10b), respectively. The control experiments demonstrated that the $[Co(tpy)_2]^{2+/3+}$ exerted a positive influence in the Z-schematic CO_2 reduction, the metal complex [Ru(dpbpy)] endowed the Z-schematic CO_2 reduction system a high reduction selectivity up to 64%. What's more, isotope tracer experiment using $^{13}CO_2$ and $H_2{}^{18}O$ demonstrated that the CO and $HCOO^-$ were originated from CO_2 with H_2O as the electron donor. The construction of a liquid-phase Z-scheme photocatalyst with functional metal complexes is a good strategy. Meanwhile, the pH value of the reaction system can impact the reactions of redox mediators, which affects their recyclability [173], thus affecting the stability of Z-scheme system. Moreover, the redox couple confines the reactions in aqueous system, which then hinders its widespread applications.

Metal phthalocyanines (MPc) with the conjugated macrocycle structure is favorable to build a dimension-matched interface with other sheet semiconductors. Besides, owing to its intense characteristic absorption in Vis-NIR regions ascribed to the

metal-ligand charge transfer (MLCT), moreover, it has been confirmed that the central metal atoms usually act as the catalytic active site of the large conjugated ring [175,176]. Therefore, they are widely applied in combining with other semiconductors with weak light absorption capacity to broaden its light capturing range. Bian *et al*. [183] successfully fabricated the ultrathin zinc phthalocyanine/graphene/$BiVO_4$ Z-scheme heterojunctions through a two-step hydroxyl-induced assembly strategy, with a 14-time CO_2 to CO activity enhancement compared to the single $BiVO_4$ nanosheet. The drastically improved photocatalytic performance was ascribed to the enhanced Z-scheme charge transfer and separation (Fig. 11a). The intrinsic 2D structured graphene with the high electrical conductivity nature endows it much preferable for the interfacial charge transfer and separation in designing 2D matched heterojunctions [183]. Moreover, graphene was used to protect ZnPc from self-aggregation by pre-treating with acids to enhance the amount of hydroxyl groups on its surfaces. The well connect with $BiVO_4$ nanosheets (BVNS) with the ZnPc was assemblied [183]. The photocatalytic activity for CO_2 reduction of the obtained samples is evaluated, and the optimized 4ZnPc/1.5G/BVNS presented much higher rate (Fig. 11b). Meanwhile, the 4ZnPc/1.5G/BVNS keeps good stability for 4 cycles in the CO_2 reduction (Fig. 11c).

3.3.3 N_2 photofixation

In natural systems, the enzyme nitrogenase can fix N_2 to NH_3. There are two proteins in the natural nitrogenase complex with the homodimeric Fe protein and the heterotetrameric MoFe protein [50,238,239]. The role of the Fe protein is to transfer electrons from a reducing reagent, such as ferredoxin or flavodoxin. The MoFe protein is mainly responsible for the supply of electrons. The binding and hydrolysis of ATP can supply energy for the electron transfer. In the Haber-Bosch process, however, nitrogen reduction for NH_3 synthesis is accomplished at a tough conditions, high pressures and temperatures over metal or metal oxides catalysts, which is low efficiency and harmful to the environment. To overcome such obstacle, Brown *et al*. [240] enlightened by nature, first used an inorganic semiconductor to mimic the role of the Fe protein in nitrogenase. The CdS was combined with the nitrogenase MoFe protein for N_2 fixation. CdS was used to photosensitize the MoFe protein, where light harvesting instead of ATP hydrolysis drives the enzymatic reduction of N_2 into NH_3 [240]. Such a successful hybrid system presented efficient N_2 fixation performance, and the turnover rate for NH_3 production reached up to 75 per minute. Under optimal conditions, about 60% of the ATP-coupled reaction rate was achieved. This work highlights the possibility of designing hybrid systems with organic and inorganic semiconductors for N_2 photofixation. As mentioned above, construction heterojunction is the preferable approach to elevate the N_2 fixation performance of g-C_3N_4 [241–244].

Recently, Liang *et al*. [245] reported the $W_{18}O_{49}$/g-C_3N_4 Z-scheme heterojunction with outstanding N_2 reduction performance under the UV to the NIR region without electron mediator. The $W_{18}O_{49}$ is appropriate for nitrogen reduction with oxygen vacancies. Moreover, $W_{18}O_{49}$ also shows intense absorption of NIR light owing to the mixed-valence W ions within its structure [245]. For the $W_{18}O_{49}$/g-C_3N_4 heterojunction, $W_{18}O_{49}$ served as the sunlight capturer, while g-C_3N_4 provided active sites for the nitrogen reduction. The NH_4^+ production rate of $W_{18}O_{49}$(0.6)/g-C_3N_4 is 2.6 $mg·L^{-1}·h^{-1}$ per gram catalyst, 7.2-fold higher than that of neat g-C_3N_4 (Fig. 12a), and the NH_4^+ production stability of $W_{18}O_{49}$(0.6)/g-C_3N_4 is excellent (Fig. 12b). The experiments of RhB photodegradation were conducted to testify the Z-scheme mechanism [245]. Additionally, there are a number of Z-scheme N_2 fixation systems consist of g-C_3N_4 and other semiconductors, such as $Mg_{1.1}Al_{0.3}Fe_{0.2}O_{1.7}$/$C_3N_4$ [241], Ga_2O_3-DBD/g-C_3N_4 [242], $CeCO_3OH$/g-C_3N_4/CeO_2 [243], MnO_{2-x}/g-C_3N_4 [244] and $Bi_4O_5Br_2$/g-C_3N_4 [246]. Nevertheless, the study of N_2 photofixation is still in its infant stage, further research to explore the underlying mechanism so as to attain excellent N_2 fixation performance is desired.

As above discussed in the applications of different type photocatalytic systems, pure inorganic semiconductors (usually displaying efficient photoactivity) and inorganic-organic hybrid systems have been widely utilized in photocatalytic energy conversion fields [247–260]. While, the organic semiconductors with a large π-conjugated stucture and adjustable photoelectric properties are key route [188,261–265]. Nevertheless, the direct utilization in energy conversion field as photocatalysts seems to be rare compared with inorganic semiconductors in the past five

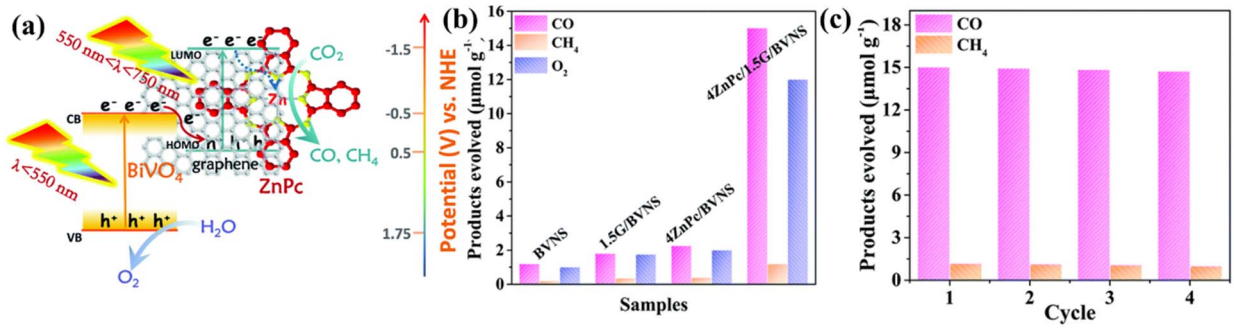

Fig. 11 (a) Z-scheme-based photogenerated charge transfer and separation. (b) Photoactivities for CO_2 reduction of BVNS, 1.5G/BVNS, 4ZnPc/BVNS, and 4ZnPc/1.5G/BVNS. (c) Cycling test with 4ZnPc/1.5G/BVNS.

Adapted and reproduced with permission [183]. Copyright 2020, The Royal Society of Chemistry.

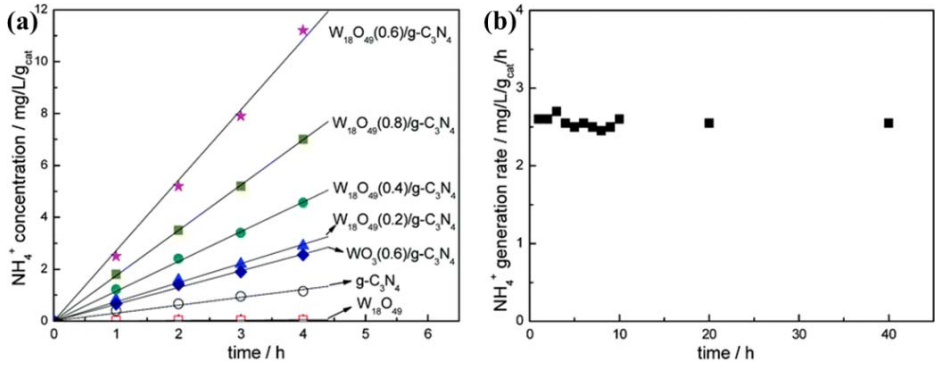

Fig. 12 (a) N_2 photofixation stability of $W_{18}O_{49}$(0.6)/g-C_3N_4. (b) NH_4^+ production ability of $W_{18}O_{49}$(0.6)/g-C_3N_4 using $AgNO_3$ as the electron scavenger [259].

years [266,267], and the novel organics, e.g., zeolitic imidazolate frameworks (ZIFs), covalent triazine-based frameworks (CTFs), azine covalent organic framework (ACOF), polymeric porphyrin and polyphthalocyanine also have large development space. On the other hand, compared to photocatalytic water splitting, there are fewer reports on CO_2 reduction, N_2 fixation and other application using pure organic polymer semiconductors, most likely due to the inherent higher requirements of kinetic and energetic challenges in CO_2 reduction and N_2 fixation reactions. On the whole, pure inorganic semiconductor system and inorganic-organic hybrid systems have made great progress in the field of photocatalytic energy conversion, while more attention still need to be pureed into the photocatalytic application of organic polymer semiconductors. The summary of various Z-scheme photocatalysts and their corresponding performance are listed in Table 1.

4 Basic strategies for improving the photocatalytic performance

Photocatalytic reaction based on semiconductors is an environment friendly and sustainable technology, but the low efficiency of capturing solar energy, fast charge recombination and low efficient facial reaction rate limit the feasibility in practical application. Therefore, various controlling/engineering strategies (such as extending spectral absorption region, promoting charge separation/transfer and surface chemical modification) have been used to improve the photocatalytic performance of Z-scheme photocatalytic systems.

4.1 Extending spectral absorption region

As mentioned above, UV light occupies less than ~5% of the all solar energy spectrum, wide bandgap photocatalysts (E_g > 3.0 eV) cannot be provoked for efficient solar energy harvesting and conversion. To further extend the solar light absorption range, tailoring the bandgap *via* metal/non-metal ion doping, organic dyes or narrow bandgap semiconductor sensitizers which can act as elegant architectures mimicking the light harvesting antenna and localized surface plasmon resonance effect are preferable methods [190,191,268–270].

4.1.1 Photosensitization

Using a visible-light dye which can sensitized to the wide bandgap oxide semiconductor has been studied for decades since the pioneering work of Gerischer in photoelectrochemistry [192]. It is still an big challenge to using a dye-sensitized oxide photocatalyst for efficient overall water splitting. On one hand, the use of organic dyes as sensitizers suffers from their poor stability since they readily decompose under long time irradiation. On the other hand, photocorrosion may happened in the narrow bandgap semiconductor. The appropriate photosensitizer is vital for enhancing the photon absorption of the Z-scheme systems [193].

By combining the dye-sensitized semiconductor with other materials to construct Z-scheme system can remarkably boost the water splitting performance. Oshima *et al.* [191] reported an efficient dye-sensitized Z-scheme system for overall water splitting using modified $HCa_2Nb_3O_{10}$ nanosheets sensitized by Ru(II) complex with a WO_3-based OER photocatalyst (Fig. 13), whereby Pt as HER cocatalyst was deposited both in the interlayer galleries and on the external surface of restacked $HCa_2Nb_3O_{10}$ nanosheets, and PtO_x as OER cocatalyst was deposited on WO_3 using H_2PtCl_6 as a precursor followed by an anneal process. Due to the efficient hole-electron pairs transport, this system displays outstanding overall water splitting efficiency with an AQY of 2.4% at 420 nm, which is the highest one among those dye-sensitized systems.

4.1.2 Localized surface plasmon resonance (LSPR) effect

In the control engineering of semiconductor's energy band structure, there is a contradiction between reducing the band gap to obtain a wider spectral responsive range and preserving the redox ability of photoexcited charge carriers of semiconductors. Fortunately, plasmonic photocatalysts can simultaneously keep the redox ability of charge carriers and extend the light absorption range based on localized surface plasmon resonance (LSPR) effect, which is derived from the electron cloud on metal (such as Au, Ag, Cu) nanoparticles oscillation in resonance with the electric field of the incident light [194]. It offers good ways to extending the absorption of the photocatalysts. Usually, LSPR

Table 1 Summary of various representative Z-scheme heterojunctions and their photocatalytic performance for energy conversion.

Photocatalyst	Dosage, light source [a]	Photoreaction solution	Activity [b], AQY or STH (%)	Ref.
Inorganic Z-scheme photocatalyst				
Overall water splitting or HER				
BP/$BiVO_4$	5 mg, λ > 420 nm	Pure water	H_2: 160, O_2: 100, AQY: 0.89% at 420 nm	70
TiO_2/NiS	50 mg, 350 Xe-lamp	Methanol aqueous solution	H_2: 655	104
Ag_2S/WO_3	15 mg, full spectrum	Lactic acid aqueous solution	H_2: 32.9	105
Co_9S_8/CdS	1 mg, λ > 400 nm	Benzyl-alcohol aqueous solution	H_2: 10321	106
ZnO_{1-x}/$Zn_{0.2}Cd_{0.8}S$	100 mg, λ > 420 nm	Na_2S + Na_2SO_3 solution	H_2: 25180, AQY: 49.5% at 420 nm	107
In_2O_3/$ZnIn_2Se_4$-Mo	20 mg, λ > 420 nm	Na_2S + Na_2SO_3 solution	H_2: 6950	110
CdS/$CdWO_4$	10 mg, λ > 420 nm	Na_2S + Na_2SO_3 solution	H_2: 2400	111
TiO_2/CdS	0.1 mg, one sun (97 mW·cm^{-2})	Pure water	H_2: 0.60 μmol·h^{-1}, STH: 0.031%,	112
g-MnS/Cu_7S_4	1.0 mg, full spectrum	Na_2S + Na_2SO_3 aqueous solution	H_2: 718	113
Au/Pt/WO_3/TiO_2	50 mg, full spectrum	Methanol aqueous solution	H_2: 242.09	116
WO_3/TiO_2	0.1 g, 35 W Xe HID H-7 lamp	Glycerol aqueous solution	H_2: 0.0172 h^{-1}·g^{-1}	117
BP/RP	2 mg, λ > 420 nm (LED lamp)	Pure water	H_2: 2960, AQY: 1.21% at 420 nm	118
Ru/$SrTiO_3$:La,Rh/$BiVO_4$:Mo	20 mg, λ > 420 nm	Pure water	H_2: 3200, O_2: 1600, AQY: 19% at 419 nm	119
Pt/$CuGaS_2$/RGO/$BiVO_4$/CoO_x [c]	100 mg, λ > 420 nm	Pure water	H_2: 35, O_2: 17	120
$MgTa_2O_{6-x}Ny$/TaON/PtO_x-WO_3	225 mg, λ > 420 nm	IO_3^-/I^- aqueous solution (pH6.1)	H_2: 480, O_2: 250, AQY: 6.8% at 420 nm	121
MoS_2/CdS, Co_3O_4/$BiVO_4$	100 mg, λ > 420 nm	Pure water	H_2: 145, O_2: 71, AQY: 1.04% at 420 nm	122
$BiVO_4$-ZrO_2/TaON	100 mg, λ > 420 nm	$[Fe(CN)_6]^{4-}$ /$[Fe(CN)_6]^{3-}$ solution	H_2: 1300, O_2: 650, AQY: 10.3% at 420 nm	123
$SrTiO_3$:La,Rh/Au/$BiVO_4$:Mo	7.5 cm^2, λ > 420 nm	Pure water	H_2: 145, O_2: 71, STH: 1.1%, AQY: 33% at 419 nm	124
Au/CoO_x-$BiVO_4$/$RhyCr_{2-y}O_3$-ZrO_2/TaON	100 mg, λ > 420 nm	$K_4[Fe(CN)_6]$ aqueous solution	H_2: 130, O_2: 65, AQY: 1.04% at 420 nm	125
$ZnIn_2S_4$/Au/TiO_2	50 mg, full spectrum	Pure water	H_2: 186.3, O_2: 66.3	126
Pt/$(CuGa)_{0.5}ZnS_2$/RGO-(CoO_x/ $BiVO_4$)	150 mg, λ > 420 nm	Pure water	H_2: 266, O_2: 133, AQY: 0.8% at 440 nm	127
CO_2 reduction				
CdS/WO_3	100 mg, λ > 420 nm	CO_2 and H_2O vapor	CH_4: 1.02	6
CdS/TiO_2	–, Full spectrum	CO_2 and H_2O vapor	CH_4: 11.9 mmol·g^{-1}·m^{-2}	83
$Fe_2V_4O_{13}$/RGO/CdS	25 mg, λ > 420 nm	CO_2 and H_2O vapor	CH_4: 2.04, O_2: 3.9	128
CdS NSs/RGO/TiO_2	25 mg, full spectrum	CO_2 and H_2O vapor	CH_4: 0.189, O_2: 0.111	129
α-Fe_2O_3/Cu_2O	100 mg, λ > 400 nm	CO_2 and H_2O vapor	CO: 1.67, O_2: 0.83	130
SiC/MoS_2	10 mg, λ > 420 nm	CO_2 and H_2O vapor	CH_4: 323, O_2: 621, AQY: 1.75% at 400 nm	131
Cu_2O/WO_3	85 mg, λ > 400 nm	CO_2 and H_2O vapor	CO: 0.49, H_2: 0.03, O_2: 0.24 (24 h)	132
WO_3/Au/In_2S_3	10 cm^2, λ > 420 nm	CO_2 and H_2O vapor	CH_4: 0.42	133
$BiVO_4$/C/Cu_2O [d]	1cm^2, λ > 420 nm	CO_2 and H_2O vapor	CO: 3.01	134
$ZnIn_2S_4$/TiO_2	100 mg, full spectrum	CO_2 and H_2O vapor	CH_4: 1.135	135
WO_3-TiO_2/Cu_2ZnSnS_4	100 mg, λ > 420 nm	CO_2 and H_2O vapor	CH_4: 15.37, CO: 1.69	136
CdS/BiOI	20 mg, λ > 420 nm	CO_2 and H_2O vapor	CH_4: 0.18, CO: 1.11	137
Cu_2O/TiO_2	30 mg, λ > 380 nm (Hg-lamp)	CO_2 and H_2O vapor	CO: 2.21	138
N_2 fixation				
TiO_2/$ZnFe_2O_4$	250 Xe-lamp	N_2, methanol aqueous solution	NH_4^+: 1.48 μmol·L^{-1}·min^{-1}	139
Organic Z-scheme photocatalyst				
Overall water splitting or HER				
aza-CMP/RGO/C_2N	50 mg, λ > 420 nm	Pure water	H_2: 200, O_2: 100, STH = 0.23%	125
Ao-TST@CMP (2D COFs)	–, –	Pure water	AQY: 20.6% (theoretically calculated value)	218
PANI-Ag-CN	15 mg, 500W Xe-lamp	Triethanolamine solution	H_2: 5048	219
CFB/NH_2-MIL-125(Ti)	20 mg, λ > 420 nm	Triethanolamine solution	H_2: 1123	220
Inorganic-organic hybrid Z-scheme photocatalyst				
Overall water splitting or HER				
g-C_3N_4/$W_{18}O_{49}$	5 mg, full spectrum	TEOA	H_2: 3040	161
ZnO/ZnS/g-C_3N_4	100 mg, full spectrum	Na_2S + Na_2SO_3 aqueous solution	H_2: 301	167

to be continued

continued Table 1

Photocatalyst	Dosage, light source [a]	Photoreaction solution	Activity [b], AQY or STH (%)	Ref.
g-C_3N_4/Ti^{3+}-TiO_2	100 mg, λ > 400 nm	CH_3OH	H_2: 287	168
g-C_3N_4/Zn/$BiVO_4$	150 mg, λ > 420 nm	Fe^{3+}/Fe^{2+} aqueous solution	H_2: 1467, O_2: 733	169
PtO_x/CrTPPCl/KTa(Zr)O_3	50 mg, 500W Xe-lamp	Pure water	H_2: 1026, O_2: 514	170
P10/$BiVO_4$ [c]	54 mg, λ > 420 nm	Fe^{2+}/Fe^{3+} aqueous solution	H_2: 92.5, O_2: 50	171
RuP/Al_2O_3/Pt(in)/$HCa_2Nb_3O_{10}$, PtO_x/H-Cs-WO_3 [f]	70 mg, λ > 420 nm	NaI aqueous solution (pH4.0)	H_2: 542.6, O_2: 236, AQY: 2.4% at 420 nm	191
a-Fe_2O_3/g-C_3N_4	10 mg, λ > 400 nm	TEOA	H_2: 30000, AQY: 44.35% at 420 nm	200
a-Fe_2O_3/TpPa-2-COF	10 mg, λ > 420 nm	Sodium ascorbate	H_2: 3770	227
CdS/g-C_3N_4	50 mg, λ > 420 nm	TEOA	H_2: 2563	257
Pt-CN/HWO	50 mg, λ > 420 nm	TEOA	H_2: 17240, AQY: 17.5% at 400 nm	258
Mo_2C/Mo/g-C_3N_4	5 mg, λ > 420 nm	TEOA	H_2: 219.7	259
g-C_3N_4/ZnO	100 mg, full spectrum	CH_3OH	H_2: 152.7	260
Cu_3P/g-C_3N_4	10 mg, λ > 420 nm	TEOA	H_2: 808	232
CdS/Au/TiO_2	50 mg, 750 W Xe-lamp	Na_2S + Na_2SO_3 aqueous solution	H_2: 64	247
CO_2 reduction				
CoZnAl-LDH/RGO/g-C_3N_4	50 mg, full spectrum	CO_2 and H_2O vapor	CO: 10.11, AQY: 0.45% at 385 nm	80
COF-318-TiO_2	2 mg, λ = 380–800 nm	CO_2 and H_2O vapor	CO: 69.67	82
RuRu'/Ag/Ta_3N_5 [g]	4 mg, λ > 480 nm (400 W Hg-lamp)	CO_2 and H_2O vapor	HCOOH: 5	152
[Ru-dpbpy]-$(CuGa)_{1-x}Zn_{2x}S_2$/$BiVO_4$	8 mg, λ > 390 nm	CO_2, H_2O vapor, $[Co(tpy)_2]^{2+/3+}$ [h]	CO: 0.103, $CHOO^-$: 0.023, H_2: 0.122	174
g-C_3N_4/$Bi_4O_5I_2$	100 mg, λ > 400 nm	CO_2, H_2O vapor, I_3^-/I^- solution	CO: 45.6, CH_4: 5.6, H_2: 2.2, O_2: 9	180
UiO-66-NH_2/RGO/O-ZnO	100 mg, λ > 420 nm	CO_2 and H_2O vapor	CH_3OH: 34.83, HCOOH: 6.41	181
PCN-224(Cu)/TiO_2	–, λ > 400 nm	CO_2 and H_2O vapor	CO: 1.67, O_2: 0.83	182
ZnPc/BVNS	100 mg, λ > 420 nm	CO_2 and H_2O vapor	CO: 0.85, CH_4: 0.15	183
Ag_3PO_4/g-C_3N_4	350 mg, full spectrum	CO_2 and H_2O vapor	CO: 39.8, CH_3OH: 8.8, CH_4: 4	185
BiOBr/Au/g-C_3N_4	100 mg, λ > 380 nm	CO_2 and H_2O vapor	CO: 6.67, CH_4: 0.92	186
Porous-g-C_3N_4/Al-O/TiO_2	700 mg, full spectrum	CO_2 and H_2O vapor	CH_3OH: 45.4, CH_3COOH: 54.9, HCOOH: 42.7	187
Bi_2WO_6/RGO/g-C_3N_4	50 mg, λ > 400 nm	CO_2 and H_2O vapor	CO: 16, CH_4: 2.5, H_2: 2.25, O_2: 10.5	233
Ag_2CrO_4/NG/PI [i]	10 mg, λ > 400 nm (500 W Xe-lamp)	CO_2 and H_2O vapor	CH_3OH: 18, CH_4: 4, C_2H_5OH: 4	235
g-C_3N_4/SnS_2	50 mg, λ > 420 nm	CO_2 and H_2O vapor	CH_4: 12.8, CH_3OH: 46	237
N_2 fixation				
$Mg_{1.1}Al_{0.3}Fe_{0.2}O_{1.7}$/$C_3N_4$	200 mg, λ > 400 nm (250 W Na-lamp)	N_2, ethanol aqueous solution	NH_4^+: 7.5 mg·L^{-1}·h^{-1}·g^{-1}	241
Ga_2O_3-DBD/g-C_3N_4	20 mg, full spectrum (500 W Xe-lamp)	N_2, methanol aqueous solution	NH_4^+: 112.5 μmol·L^{-1}·h^{-1}	242
$CeCO_3OH$/g-C_3N_4/CeO_2	30 mg, full spectrum (500 W Xe-lamp)	N_2, water	NH_4^+: 1.16 mmol·g^{-1}·h^{-1}	243
MnO_{2-x}/g-C_3N_4	50 mg, full spectrum	N_2, methanol aqueous solution	NH_4^+: 225 μmol·g^{-1}·h^{-1}	244

[a] 300 W Xe-lamp if otherwise stated; [b] μmol·h^{-1}·g^{-1} if otherwise stated; [c] RGO: reduced graphene oxide; [d] C: conductive carbon. [e] P10: homopolymer of dibenzo[b,d]thiophene sulfone; [f] Rup: Ru(II) *tris*-diimine type photosensitizer; [g] RuRu′: binuclear Ru(II) complex; [h] tpy: 2,2′:6,2″-terpyridine; [i] PI: Polyimide.

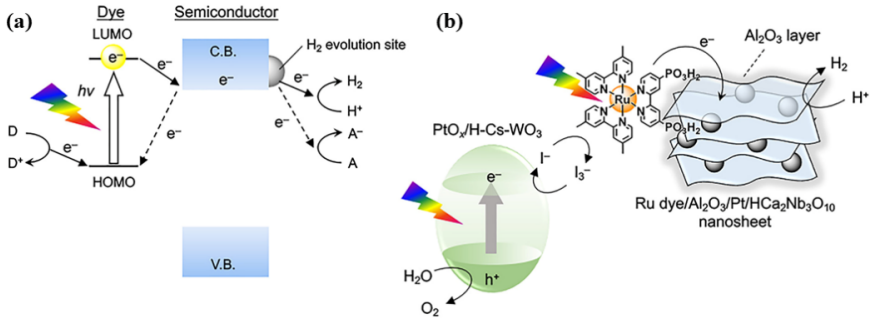

Fig. 13 (a) Electron transfer mechanism of the system. (b) Scheme of Z-scheme water splitting using Ru dye-sensitized Al_2O_3/Pt/$HCa_2Nb_3O_{10}$ and PtO_x/HCs-WO_3.

Adapted and reproduced with permission [191]. Copyright 2020, The American Chemical Society.

effect leads a high degree of light scattering and produces intense electric fields at the surface of nanoparticle, and thus causing sharp spectral absorption and scattering peaks. In addition, the resonance frequency can be tailored by altering the nanoparticle

size and shape as well as manipulating the composition of the metal nanoclusters, and the decay of LSPR can induce hot electrons and holes in the metal. In this situation, the visible light is captured by metal nanoparticals *via* LSPR instead of excitation of semiconductor due to the electrons injecting into the CB of semiconductor [195,270], which is similar to the dye sensitization. The LSPR can elevate light absorption of semiconductor along with the accompanied electron transfer [19], and thus combining the metal with LSPR effect and other semiconductor is a desired strategy to construct efficient Z-scheme systems with intense visible light absorption.

Apart from the $W_{18}O_{49}$ with active LSPR effect presenting in part of Section 3.3.1 [161,270], MOFs with especial 3D well-defined structure, substantial porosity, and large surface area are attractive [196]. Photosensitive MOFs can be excited by incident light with energy equaling to or greater than E_g, and show semiconducting properties, which can trigger various chemically desirable photo-redox reactions. Liu *et al*. [271] synthesized Ag/AgCl@MIL-53-Fe Z-scheme photocatalysts by coupling MIL-53-Fe with plasmonic Ag/AgCl, and found that the absorption intensity in the range of 300-600 nm can be improved owing to the SPR absorption of Ag nanoparticles at $\lambda > 400$ nm and the excitation of AgCl at $\lambda < 400$ nm. In addition, Ag/AgCl can promote the photogenerated charge separation. The SPR-excited electrons are transferred to AgCl *via* Schottky barrier. In the meantime, MIL-53-Fe is excited under visible light and gives photoexcited charge, and the photoexcited electrons in the MIL-53-Fe's CB would migrate to Ag particles, leading to the accumulation of holes in the VB of MIL-53-Fe. Moreover, the intrinsic porosity and large surface area of MOFs provide open channels for good reactant diffusion to improve the photocatalytic activity, and the SPR effect of metallic Ag plays a vital role in boosting the charge transfer and elevating the photocatalytic performance of the Z-scheme system [271].

4.2 Promoting the charge separation/transfer

Constructing hybrid structures or multicomponent photocatalysts has been proven as a useful way toward high photocatalytic performance. Interfacial charge transfer/separation have been deemed as an essential factor remarkably influencing the photocatalytic performance. While, the charge transfer/separation between the hybrid semiconductors can be tailored according to the following aspects:

4.2.1 Shorter charge migration distance

Due to the minimized diffusion distance and depressed charge recombination, 2D materials have been widely used in the photocatalytic field. Comparing with other heterojunction (0D/0D, 0D/1D, 0D/2D, 1D/1D, 1D/2D), 2D/2D heterojunction with large contacting interfaces is a desirable strategy to shorten the charge migration distances [125,197–200]. For example, the above aza-fused CMP and C_2N nanosheets formed 2D/2D polymer Z-scheme heterojunction photocatalysts, fabricated by Wang *et al*. [125], presented efficient and stable overall water splitting activity. Similarly, a sandwich-like 2D hybrid structure composed of g-C_3N_4 and α-Fe_2O_3 nanosheets were fabricated *via* one-step growth approach (Fig. 14a) [200]. The assembled α-Fe_2O_3/2D g-C_3N_4 hybrid has an obvious interface between α-Fe_2O_3 and 2D g-C_3N_4 nanosheets (Fig. 14b), and the band alignment between 2D g-C_3N_4 and α-Fe_2O_3 resulted in the formation of a Z-scheme structure for overall water splitting (Fig. 14c) [200].

4.2.2 Morphology and mass (molar) ratio controlling

The morphology, such as the smaller particle size or higher crystallinity are helpful to the performance. Proper control of morphology can enhance the photocatalytic performance of Z-scheme systems [104,125,131,183,247]. One active example is the architecture CdS/Au/TiO_2 system. The black butterfly wing was studied by Ding *et al*. [247] The scale and discovered quasi-honeycomb (QH) morphology could remarkably increase the light capture ability, and the fabricated CdS/Au/TiO_2 with wing architecture exhibited a 230% increase in light capture ability as compared with the plate architecture based TiO_2, suggest that morphology is important [247].

Also, the photogenerated electrons from the CB of one semiconductor require an equivalent number of photogenerated holes from the VB of another semiconductor. Therefore, the mass ratio between the two semiconductors should be optimized [104,125,131,183]. Two types of photogenerated charge carriers will be imbalanced, and the excess electrons and holes will recombine with their counter-parts in the bulk or reduce/oxidize the photocatalyst itself, that is photocorrosion.

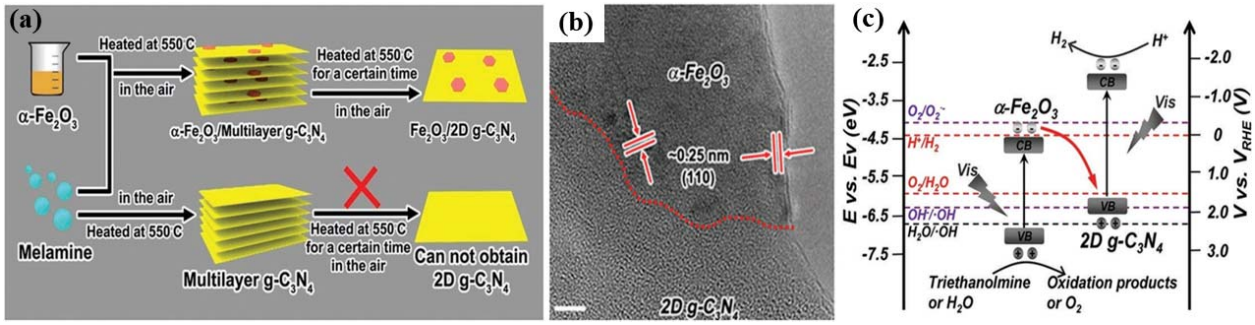

Fig. 14 (a) The synthetic route to produce the α-Fe_2O_3/2D g-C_3N_4 hybrids. (b) HRTEM image of the α-Fe_2O_3/2D g-C_3N_4 (3.8%) hybrid. (c) Energy band diagram of α-Fe_2O_3/2D g-C_3N_4 hybrids at pH = 0.

Adapted and reproduced with permission [200]. Copyright 2017, Wiley.

Thus, they would adverse to the Z-scheme photocatalytic reaction, while optimizing the mass (molar) ratio of the components can restrain the above negative impacts.

4.3 Surface chemical modification

Light absorption, charge separation/transfer and surface chemical reactions determine the overall efficiency of photocatalytic systems [253–270], and the surface redox reactions can be optimized by cocatalyst loading and other surface modification approach [271–281].

4.3.1 Cocatalyst

Among the photocatalyst designs, loading of cocatalyst on semiconductor to form hybrid structures is a good approach to facilitate the surface chemical reaction efficacy of photocatalysts [154]. In photocatalytic reactions, cocatalysts are not the light-harvesting components. Instead, cocatalysts plays the following key roles in photocatalytic process [271–273]: (1) Reducing the activation energy or overpotential for the surface reactions; (2) Boosting the separation and migration of photoinduced hole-electron pairs in Z-scheme systems; (3) Enhancing the directional redox reactions efficiency and selectivity; (4) Maintaining the stability and lowering the possibility of photocorrosion of semiconductors by timely extracting the photogenerated charge; (5) Suppressing the side and back reactions. Besides, cocatalysts acting as alternative reaction sites can retard the photocorrosion of semiconductor resulted from the charge accumulation and thus improve the photostability. Therefore, loading cocatalysts on the semiconductor is common in the photocatalysis field [219,271–284].

According to the nature of trapped charge carriers, cocatalysts can be divided into two categories: the reduction cocatalyst capturing electrons for the reduction half reactions, and the oxidation cocatalyst capturing holes for the oxidation half reactions. Generally, noble metals (e.g., Pt, Ag, Pd and Rh) [271,274,275], some transition metals (e.g., Cu, Fe, Co and Ni) [192], and metal sulfides (e.g., MoS_2, NiS) [276,277] can serve as reduction cocatalysts. Among the noble metal cocatalysts, Pt has the highest work function (5.65 eV) [219], indicating the robust electron-extracting capacity, and thus Pt demonstrates outstanding performance in the reductive reactions. Besides, some novel reductive cocatalysts such as Mo-rich molybdenum carbide (Mo-Mo_2C) [254], Ni_2P [272], carbon-coated cubic molybdenum carbide (MoC@C) [282], S^{2-}-adsorbed MoS_x [283] and Pt-M (M = Co, Ni, Fe) alloy [284] *et al.* have also been supposed, which provide alternatives for designing efficient and low-cost Z-scheme photocatalytic systems. The oxidation half reaction is the primary reaction of both water splitting and CO_2 reduction reactions, which determines the overall performance of the two type reactions. The multi-electrons were involved in the oxidation half reactions, thus loading of effective oxidation cocatalysts can drastically enhance the OER rate and improve the total efficiency of Z-scheme systems. Moreover, transitional metal oxides (e.g., CoO_x, RuO_x and PtO_x) and phosphates (e.g., CoP) have been extensively utilized for water oxidation [279,280]. It's worth noting that the loading dosage and the type of cocatalyst remarkably influence the photocatalytic activity. For example, when different content of Co cocatalyst was loaded on BP/RP hetero-phase junctions [192], the H_2 production activity increases with the increase of Co content, and then decreases gradually once the loading dosage excesses the optimal amount (1.42%). On the one hand, excessive cocatalyst has the negative light-shielding effect, resulting in a lower light adsorption ability of semiconductor. On the other hand, excessive cocatalyst will occupy the reaction active sites, which adverse to the surface chemical reactions. Apart from loading dosage, the type of the cocatalyst distinctly impact the performance of photocatalyst, and therefore cocatalyst should be carefully optimized [192].

Since the electrons and holes are usually migrating to different positions on the photocatalyst surface, the reductive and oxidative cocatalysts can be used. For instance, Iwase *et al.* [120] demonstrated powdered Z-schematic water splitting by using metal sulfides as HER photocatalyst, RGO as an electron mediator, and $BiVO_4$ as OER photocatalyst (Fig. 15a). Whereby Pt served as the HER cocatalyst, and the cobalt oxide (CoO_x) as OER cocatalyst, so that H_2 and O_2 evolved steadily [120]. The metal Pt can reduce the overpotential of HER, thus promoting the water reduction activity. In addition, only a few H_2 was produced owing to the photocorrosion without CoO_x (Fig. 15b), indicating that the main factor for the Z-scheme system with the CoO_x-cocatalyst on $BiVO_4$. Besides, the system also exhibited CO_2 reduction performance (Fig. 15c). This work provides reference

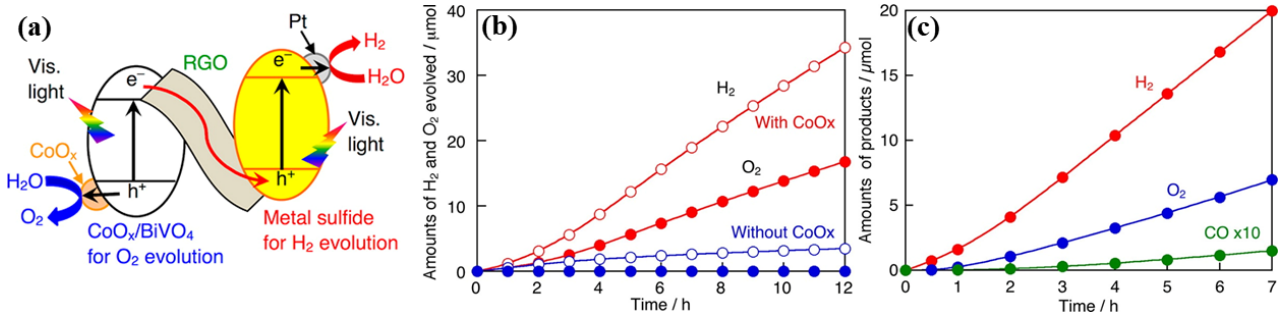

Fig. 15 (a) The Pt-loaded metal sulfide photocatalyst and an RGO-CoO_x/$BiVO_4$ composite photocatalyst. (b) The rate of Pt/$CuGaS_2$ and an RGO (5% (*w*)-$BiVO_4$ composite. (c) The rate of $CuGaS_2$ and an RGO (5% (*w*))-CoO_x/$BiVO_4$ composite.

Adapted and reproduced with permission [120]. Copyright 2016, The American Chemical Society.

to the artificial photosynthetic systems using metal sulfide.

Cocatalyst can be applied in various photocatalytic applications mentioned above, and therefore the selection of desired cocatalyst for different photocatalytic reactions is necessary. Since those artificial photosynthetic systems such as water photosplitting, CO_2 photoreduction and N_2 photofixation usually involve the same oxidation half reaction that need oxidative cocatalyst, the reductive cocatalyst should be carefully selected for different systems based on the following reasons: (1) Photocatalytic activity. The cocatalysts that can remarkably boost the photoactivity should be preferentially considered in different photocatalytic applications. (2) Photocatalytic selectivity. As for water photosplitting, there is only one reduction half reaction for H_2 evolution, and Pt, Pd, Rh, Au, Cu, Co, Ni, NiS, NiO, Co_2P, NiP, graphene and even carbon nanotube can act as the reductive cocatalyst. In CO_2 photoreduction and N_2 photofixation, the photocatalytic reduction reactions of CO_2 and N_2 are harder than water splitting, and the corresponding products are more complicated. Hence, the cocatalyst which can remarkably lower the adsorption/activation energy of the reactants (CO_2/N_2/H_2O) and promote the formation and desorption processes of various corresponding products (CO, CH_4, CH_3OH, HCOOH, C_2H_5OH or NH_3) is highly desired. Generally, Pt, Pd, Ag, NiO, RuO_2 can be utilized in CO_2 photoreduction, and Pt, Ru and black phosphorus nanosheets can be utilized in N_2 photofixation [278,284]. In addition, the selectivity of product induced by cocatalyst is different. For example, Pt is the best cocatalyst for trapping electrons for inducing the water reduction half reaction because of the largest work function among the noble metals, while the selectivity order of noble metals for CO_2 photoreduction is Ag > Au > Pd > Pt [285]. Therefore, Ag instead of Pt is commonly used in the CO_2 photoreduction system. That is, it is necessary to select suitable cocatalysts according to the target photocatalytic applications. (3) Stability. The cocatalyst which can suppress the photocorrosion and improve the stability of photocatalyst will be more attractive.

Although the photocatalysts decorated by cocatalyst have made great development, there still are several issues to be addressed: (1) The expansion of novel noble-metal-free cocatalysts. The practical utilization of noble metals is limited by their either high cost or toxicity even though they are proved to be excellent cocatalysts; (2) The designing of the interface between photocatalyst and cocatalyst. Because of the cocatalyst surface is the site for redox reactions, it can be the key for the activity or selectivity of photoreactions. Furthermore, the interface influences the charge separation and migration processes; (3) The loading method of single cocatalyst. Different loading method (e.g., photodeposition [281,286], impregnation [287], sol-gel [288], electron spinning [288], sputtering deposition [289] and microwave-assisted deposition [290]) leads to different dispersal state, particle size and morphology of cocatalyst, thus the loading method should be deliberated for maximizing the performance of cocatalyst. Additionally, the random deposition of dual cocatalysts on the semiconductor surface is still a mainstream. Recently, selectively loading cocatalyst on the desirable reductive and oxidative sites of photocatalyst presents attractive performance, while there are still need deeply research in relative area. Last but not least, there is an optimal loading dosage of cocatalyst. The Volcano-type relationship is observed between the photocatalytic activity and cocatalyst loading (Fig. 16) [154]. The cocatalyst loaded on semiconductor could result in diminished charge recombination and enhanced reaction kinetics, and thus causing an improved photoactivity. Nevertheless, excessive cocatalyst will resulting in a drastically reduced activity because the cocatalyst shields the photocatalyst surface from incident light and introduces additional recombination centers of photoexcited charge carriers.

4.3.2 Surface chemical modification

Because photocatalytic reactions occur on the photocatalyst surface, the surface chemical environment would also impact directly the photocatalytic performance. Therefore, enormous efforts have been devoted to modify the semiconductors by surface modification. For example, Cs^+ surface modification [279,280] and the surface functional groups [220] have been developed as discussed above.

Because of the lower O_2 formation efficiency of WO_3 (quantum efficiency < 0.4 % at 405 nm) [291], numerous studies have been devoted to improve the performance of WO_3. Sayama's group [279,280] has discovered that WO_3 with surface modification following thermal treatment at 773 K using MCl (M = Na, K, Rb, and Cs) and $AgNO_3$ aqueous solutions can enhance the OER activity. Among them, Cs-treated WO_3 showed the highest activity, while a series of similar characterization results (e.g., XRD, Raman and diffuse reflection spectra) of WO_3 and Cs-WO_3 indicate that the inner structure was maintained after the surface modification. Cs-WO_3, derived from CsCl aqueous solution impregnating at 773 K for 30 min, displayed

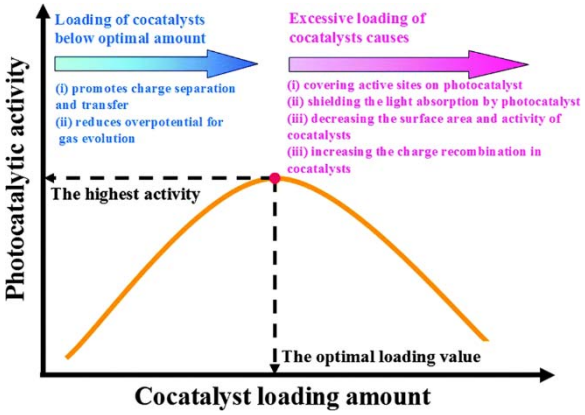

Fig. 16 Volcano-type relationship between the photocatalytic activity and the loading amount of the cocatalyst-loaded semiconductor photocatalyst.

Adapted and reproduced with permission [154]. Copyright 2014, The Royal Society of Chemistry.

the highest OER activity in the sacrificial reagent solution under $\lambda > 420$ nm light illumination [279]. The total O_2 gas amount reached *ca.* 300 mmol over Cs-WO_3, and the Fe^{2+} stoichiometric amount was determined without any Fe^{3+} after the photoreaction. The second run's activity improved with no Cs-treatment [279]. A very thin layer of cesium tungstate species formed on WO_3 surface, which has a different structure from the WO_3 bulk. The surface structure formed by Cs treatment can provide ion exchangeable sites with H^+ in acidic solutions, and the resultant H^+-ion exchanged sites can adsorb H_2O forming H_3O^+, which can be oxidize by photogenerated holes more easily, and thus the photocatalytic performance can be further enhanced *via* ion-exchange treatment with H^+ and Fe^{2+} ions, which can boost the OER photoactivity and suppress the undesirable reaction between the photoexcited holes and Fe^{2+} ions. This result on drastically promoted OER activity over WO_3 after Cs^+ aqueous solution treatment gives a novel facile way for elevating the OER performance of photocatalysts, and may provide inspiration for other photocatalytic reaction systems.

5 Summary and perspectives

In this review, the latest development of Z-scheme heterojunctions and their photocatalytic systems were illustrated with specific focuses on the progress of three types of Z-scheme photocatalysts, and the correlative strategies to improve photocatalytic performance were highlighted. The Z-scheme systems have unique advantages and could be developed to satisfy the required efficiency if all components could be optimized. However, the record STH energy conversion efficiency is only 1.2% (at 331 K under 10 kPa) derived from an all-solid-state inorganic Z-scheme (Cr_2O_3/Ru-modified $SrTiO_3$:La, Rh/C/$BiVO_4$:Mo sheets), and the organic, inorganic-organic hybrid Z-scheme heterojunctions still have large development space in the energy conversion efficiency. Although Z-scheme heterojunctions possess the most robust redox capacity and efficient charge separation, the requirements of band energy structure alignment and effective contact are tough. Besides, designing novel outstanding Z-scheme heterojunctions to achieve large-scale practical application is also highly desired. Despite the laudable advances in seeking high-efficiency and robust Z-scheme photocatalytic energy conversion systems in the last 5 years, the exploration is still at the primary stage. There are numerous challenges to overcome in the exploration of remarkably boosting activity, selectivity and long-time durable Z-scheme systems.

(1) Practical application of Z-scheme photocatalysts. Although great advance has been achieved, the diverting from laboratory-scale level to industrial applications, amplifying the yield of photocatalysts while preserving their intrinsic nature is a global challenge. Solving the following issue may be beneficial to the practical application: Reducing the cost of photocatalysis by using natural sunlight instead of the artificial light source, which is one of the key factors that the cost of photocatalysis remains high. Hence, it is crucial to develop the photocatalytic process of using natural sunlight. For efficient utilization of sunlight, researches have two trends: (i) Establishing an efficient light-harvesting system at the molecular level to absorb solar energy; (ii) Designing a better external light absorption system to get more sunlight on the photocatalysts.

(2) Repressing inevitable side and back reactions. In liquid-phase Z-scheme systems, shuttle redox pairs are indispensable to support the charge transfer. Nevertheless, the holes in HER photocatalyst and the electrons in OER photocatalyst may recombine with the redox mediator, resulting in the inactivation of redox mediators and low photocatalytic performance. Especially, some colored shuttle redox pairs (e.g., Fe^{3+}/Fe^{2+}) have light shielding effect, and thus compete with photocatalysts in light harvesting. Besides, the shuttle redox pairs sensitive to pH value can only utilized in specific conditions. Thus, traditional liquid-phase Z-scheme systems have a narrow scope of application. On the other hand, the metallic electron transfer intermedia in all-solid-state Z-scheme systems can avoid the disadvantage of shuttle redox pairs in liquid-phase Z-scheme systems, but it may act as cocatalysts rather than a charge transfer shuttle and compete with photocatalysts in light harvesting, and thus causing a low light utilization efficiency. Therefore, the charge transfer process of Z-scheme system is kinetically more challenging than the one-step system. Given that, S-scheme (step-scheme) heterojunction would be promising since the photocatalysts are classified into oxidation photocatalysts and reduction photocatalysts based on their band structure, which can reserve the effective electrons and holes while eliminating those ineffective, and thus broadening light absorption region, efficient charge separation capacity and strong redox potentials are mutually achieved. Nevertheless, further study is desired to optimize the photocatalytic performance and extend the application area of the S-scheme systems [108,184].

(3) Surface chemistry controlling and engineering. The adsorption, activation, reaction and desorption of reactant/products on the Z-scheme photocatalyst greatly limits the overall conversion efficiency and selectivity of photocatalytic systems which is a scientifically critical challenge. Especially, CO_2/N_2 adsorption and product desorption are necessary steps for the whole photocatalytic reactions, but most photocatalysts exhibit weak CO_2/N_2 adsorption/desorption performance. Developing a semiconductor with appropriate target molecule adsorption/desorption ability by designing and engineering of surface chemical properties is crucial.

(4) System mechanism (especially for CO_2 reduction and N_2 fixation). Although various active intermediate products in Z-scheme photocatalytic systems were proposed and widely investigated by various characterization techniques. The physicochemical variation, electron transfer path and multi-electron participated mechanism still need further exploration. Therefore, timely monitoring the changes in reaction processes

is essential. *In situ* or operando characterizations such as DRIFTS, *in situ* XANES, EXAFS, TEM, XPS and PL are necessary to have deep insight into the mechanisms of interfacial charge separation/transfer and the surface catalytic redox reactions. Furthermore, DFT calculations can also provide structural and electronic guidance for understanding the underlying reasons of the variations in reaction processes.

(5) Exploration of novel Z-scheme photocatalysts. Perovskite type semiconductor composites, organometallic molecules and some 2D materials (e.g., metal carbides/nitrides, metalloporphyrin and their derivatives) have demonstrated fascinating performance in photocatalytic energy conversion. Earth abundant elements with high activity, good selectivity, robust stability are always desired. Corresponding researches are still in the primary stage, which has great potential and challenges.

(6) Establishing the standard for photocatalytic performance assessment. So far, there is no standard to evaluate and compare the efficiencies of various photocatalytic systems reported in the literatures. The amount of target products per unit time depends on the photocatalyst mass, reactor setup, light source, filters, and many other factors, and thus the same material can present different activities when performed in different research groups. Currently, normalization of the evolution rate by the photocatalyst mass ($mol \cdot h^{-1} \cdot g^{-1}$) is not very appropriate, because the relationship of product generation rate and photocatalyst mass is not linear.

References

(1) Fujishima, A.; Honda, K. *Nature* **1971,** *238*, 37. doi: 10.1038/238037a0

(2) Ida, S.; Takashiba, A.; Koga, S.; Hagiwara, H.; Ishihara, T. *J. Am. Chem. Soc.* **2014,** *136*, 1872. doi: 10.1021/ja409465k

(3) Zhou, C. Y.; Lai, C.; Huang, D. L.; Zeng, G. M.; Zhang, C.; Cheng, M.; Hu, L.; Wan, J.; Xiong, W. P.; Wen, M.; *et al*. *Appl. Catal. B: Environ.* **2018,** *220*, 202. doi: 10.1016/j.apcatb.2017.08.055

(4) Marschall, R. *Adv. Funct. Mater.* **2014,** *24*, 2421. doi: 10.1002/adfm.201303214

(5) Huang, D.; Chen, S.; Zeng, G.; Gong, X. M.; Zhou, C. Y.; Cheng, M.; Xue, W. J.; Yan, X. L.; Li, J. *Coord. Chem. Rev.* **2019,** *385*, 44. doi: 10.1016/j.ccr.2018.12.013

(6) Xu, F. Y.; Xiao, W.; Cheng, B.; Yu, J. G. *Int. J. Hydrog. Energy* **2014,** *39*, 15394**.** doi: 10.1016/j.ijhydene.2014.07.166

(7) Fang, B.; Bonakdarpour, A.; Reilly, K.; Xing, Y.; Taghipour, F.; Wilkinson, D. *ACS Appl. Mater. Interfaces* **2014,** *6*, 15488. doi: 10.1021/am504128t

(8) Putri, L.; Ng, B. J.; Er, C. C.; Ong, W. J.; Chang, W. S.; Mohamed, A. R.; Chai, S. P. *Appl. Surf. Sci*. **2020,** *504*, 144427. doi: 10.1016/j.apsusc.2019.144427

(9) Tang, J. Y.; Kong, X. Y.; Ng, B. J.; Chew, Y. H.; Mohamed, A.; Chai, S. P. *Catal. Sci. Technol*. **2019,** *9*, 2335. doi: 10.1039/C9CY00449A

(10) Bard, A. *J. Photochem.* **1982,** 327. doi: 10.1016/0047-2670(82)87022-6

(11) Low, J. X.; Yu, J. G.; Jiang. C. J. *Interface Sci. Technol.* **2020,** *31*, 193. doi: 10.1016/B978-0-08-102890-2.00006-3

(12) Tada, H.; Mitsui, T.; Kiyonaga, T.; Akita, T.; Tanaka. K. *Nat. Mater*. **2006,** *5*, 782. doi: 10.1038/nmat1734

(13) Lu, Z. Y.; Yu, Z. H.; Dong, J. B.; Song, M. S.; Liu, Y.; Liu, X. L.; Ma, Z. F.; Su, H.; Yan, Y. S.; Huo. P. W. *Chem. Eng. J.* **2018,** *337*, 228. doi: 10.1016/j.cej.2017.12.115

(14) Zhao, S.; Zhang, Y. W.; Zhou, Y. M.; Fang, J. S.; Wang, Y. Y.; Zhang, C.; Chen, W. X. *J. Mater. Sci.* **2018,** *53*, 6008. doi: 10.1007/s10853-018-1995-z

(15) Low, J.; Jiang, C.; Cheng, B.; Wageh, S.; Al-Ghamdi, A.; Yu, J. G. *Small Methods* **2017,** *1*, 1700080. doi: 10.1002/smtd.201700080

(16) Jo, W.; Selvam. N. *Chem. Eng. J.* **2017,** *317*, 913. doi: 10.1016/j.cej.2017.02.129

(17) Yu, J. G.; Wang, S. H.; Low, J. X.; Xiao, W. *Phys. Chem. Chem. Phys.* **2013,** *15*, 16883. doi: 10.1039/C3CP53131G

(18) Wang, Z.; Li, C.; Domen, K. *Chem. Soc. Rev.* **2019,** *48*, 2109. doi: 10.1039/C8CS00542G

(19) Wang, Q.; Domen, K. *Chem. Rev.* **2020,** *120*, 919. doi: 10.1021/acs.chemrev.9b00201

(20) Wang, Y.; Suzuki, H.; Xie, J.; Tomita, O.; Martin, D.; Higashi, M.; Kong, D.; Abe, R.; Tang, J. *Chem. Rev.* **2018,** *118*, 5201. doi: 10.1021/acs.chemrev.7b00286

(21) Wang, J.; Wang, G. H.; Wei, X. H.; Liu, G.; Li, J. *Appl. Surf. Sci.* **2018,** *456*, 666. doi: 10.1016/j.apsusc.2018.06.182

(22) Li, H. J.; Tu, W. G.; Zhou, Y.; Zou, Z. G. *Adv. Sci*. **2016,** *3*, 1500389. doi: 10.1002/advs.201500389

(23) Guo, L. J.; Wang, Y. J.; He, T. *Chem. Rev.* **2016,** *16*, 1918. doi: 10.1002/tcr.201600008

(24) Zhang, G. J.; Su, A.; Qu, J. W.; Xu, Y. *Mater. Res. Bull.* **2014,** *55*, 43. doi: 10.1016/j.materresbull.2014.04.012

(25) Ghadimkhani, G.; de Tacconi, N. R.; Chanmanee, W.; Janaky, C.; Rajeshwar. K. *Chem. Commun*. **2013,** *49*, 1297. doi: 10.1039/C2CC38068D

(26) Truong, Q.; Liu, J.; Chung, C.; Ling, Y. *Catal. Commun.* **2012,** *19*, 85. doi: 10.1016/j.catcom.2011.12.025

(27) Bessekhouad, Y.; Robert, D.; Weber, J. *J. Photochem. Photobiol. A* **2004,** *163*, 569. doi: 10.1016/j.jphotochem.2004.02.006

(28) Liu, B. S.; Wu, H.; Parkin, I. *ACS Omega* **2020,** *5*, 14847. doi: 10.1021/acsomega.0c02145

(29) Ng, B.; Putri, L.; Kong, X.; Teh, Y. W.; Pasbakhsh, P.; Chai, S. P. *Adv. Sci.* **2020,** *7*, 1903171. doi: 10.1002/advs.201903171

(30) Zhou, L.; Boyd, C. E. *Aquaculture* **2016,** *450*, 187.

doi: 10.1016/j.aquaculture.2015.07.022

(31) Wu, N. Q.; Wang, J.; Tafen, D.; Wang, H.; Zheng, J. G.; Lewis, J.; Liu, X. G.; Leonard, S. S.; Manivannan, A. *J. Am. Chem. Soc.* **2010,** *132*, 6679. doi: 10.1021/ja909456f

(32) Liu, G.; Niu, P.; Sun, C. H.; Smith, S.; Chen, Z. G.; Lu, G.; Cheng, H. M. *J. Am. Chem. Soc.* **2010,** *132*, 11642. doi: 10.1021/ja103798k

(33) Chen, X.; Li, N.; Kong, Z.; Ong, W. J.; Zhao, X. J. *Mater. Horiz.* **2018,** *5*, 9. doi: 10.1039/C7MH00557A

(34) Bazhenova, T.; Shilov, A. *Coord. Chem. Rev.* **1995,** *144*, 69. doi: 10.1016/0010-8545(95)01139-G

(35) Van der Ham, C.; Koper, M.; Hetterscheid, D. *Chem. Soc. Rev.* **2014,** *43*, 5183. doi: 10.1039/C4CS00085D

(36) Sun, S. M.; Li, X. M.; Wang, W. Z.; Zhang, L.; Sun, X. *Appl. Catal. B: Environ.* **2017,** *200*, 323. doi: 10.1016/j.apcatb.2016.07.025

(37) Inoue, T.; Fujishima, A.; Konishi, S.; Honda, K. *Nature* **1979,** *277*, 637. doi: 10.1038/277637a0

(38) Zhang, L.; Zhao, Z. J.; Wang, T.; Gong, J. L. *Chem. Soc. Rev.* **2018,** *47*, 5423. doi: 10.1039/C8CS00016F

(39) Maeda, K. *Adv. Mater.* **2019,** *31*, 1808205. doi: 10.1002/adma.201808205

(40) Remiro-Buenamañana, S.; García, H. *ChemCatChem* **2019,** *11*, 342. doi: 10.1002/cctc.201801409

(41) Ghoussoub, M.; Xia, M.; Duchesne, P.; Segal, D.; Ozin, G. *Energy Environ. Sci.* **2019,** *12*, 1122. doi: 10.1039/C8EE02790K

(42) Sun, Z.; Talreja, N.; Tao, H.; Texter, J.; Muhler, M.; Strunk, J.; Chen, J. *Angew. Chem. Int. Ed.* **2018,** *57*, 7610. doi: 10.1002/anie.201710509

(43) Xie, J. F.; Zhao, X. T.; Wu, M. X.; Li, Q. H.; Wang, Y.; Yao, J. B. *Angew. Chem. Int. Ed.* **2018,** *130*, 9788. doi: 10.1002/anie.201802055

(44) Yang, H. P.; Wu, Y.; Lin, Q.; Fan, L. D.; Chai, X. Y.; Zhang, Q. L.; Liu, J. H.; He, C. X.; Lin, Z. Q. *Angew. Chem. Int. Ed.* **2018,** *130*, 15702. doi: 10.1002/anie.201809255

(45) Habisreutinger, S. N.; Schmidt-Mende, L.; Stolarczyk, J. K. *Angew. Chem. Int. Ed.* **2013,** *52*, 7372. doi: 10.1002/anie.201207199

(46) Gao, X. M.; Shang, Y. Y.; Liu, L. B.; Fu, F. *J. Catal.* **2019,** *371*, 71. doi: 10.1016/j.jcat.2019.01.002

(47) Li, J.; Niu, A. P.; Lu, C. J.; Zhang, J. H.; Junaid, M.; Strauss, P.; Xiao, P.; Wang, X.; Ren, Y. W.; Pei, D. S. *Chemosphere* **2017,** *168*, 112. doi: 10.1016/j.chemosphere.2016.10.048

(48) Schlogl, R. *Angew. Chem. Int. Ed.* **2003,** *42*, 2004. doi: 10.1002/anie.200301553

(49) Schrauzer, G. N.; Guth, T. D. *J. Am. Chem. Soc.* **1977,** *99*, 7189. doi: 10.1021/ja00464a015

(50) Hoffman, B.; Lukoyanov, D.; Yang, Z.; Dean, D.; Seefeldt, L. *Chem. Rev.* **2014,** *114*, 4041. doi: 10.1021/cr400641x

(51) Huang, Y. W.; Zhang, N.; Wu, Z. J.; Xie, X. Q. *J. Mater. Chem. A* **2020,** *8*, 4978. doi: 10.1039/C9TA13589H

(52) Huang, D. L.; Tang, Z. H.; Peng, Z. W.; Lai, C.; Zeng, G. M.; Zhang, C.; Xu, P.; Cheng, M.; Wan, J.; Wang, R. Z. *J. Taiwan Inst. Chem. E* **2017,** *77*, 113. doi: 10.1016/j.jtice.2017.04.030

(53) Acar, C.; Dincer, I.; Zamfirescu, C. *Int. J. Energy Res.* **2014,** *38*, 1903. doi: 10.1002/er.3211

(54) Huang, D. L.; Wang, Y.; Zhang, C.; Zeng, G. M.; Lai, C.; Wan, J.; Qin, L.; Zeng, Y. L. *RSC Adv.* **2016,** *6*, 73186. doi: 10.1039/C6RA11850J

(55) Chi, Z.; Chen, H.; Chen, Z.; Zhao, Q.; Chen, H.; Weng, Y. X. *ACS Nano* **2018,** *12*, 8961. doi: 10.1021/acsnano.8b02354

(56) Li, K.; Peng, B. S.; Peng, T. Y. *ACS Catal.* **2016,** *6*, 7485. doi: 10.1021/acscatal.6b02089

(57) Standard Test Methods for Ammonia Nitrogen in Water. ASTM D1426-15, Available online: https://www.astm.org/Standards/D1426.htm (accessed on November 24, 2020).

(58) Standard Test Method for Determination of Dissolved Alkali and Alkaline Earth Cations and Ammonium in Water and Wastewater by Ion Chromatography. ASTM D6919-09, Available online: https://www.astm.org/DATABASE.CART/HISTORICAL/D6919-09.htm (accessed on November 24, 2020).

(59) Dissolved Sodium, Ammonium, Potassium, Magnesium and Calcium in Wet Deposition by Chemically Suppressed Ion Chromatography. Method 300.7 EPA, Cincinnati, OH, US 1986.

(60) Standard Method for the Examination of Water and Wastewater, 20th ed., APHA, Washington, DC, US 2005.

(61) Crosby, N. T. *Analyst* **1968,** *93*, 406. doi: 10.1039/AN9689300406

(62) Grasshoff, K.; Johannsen, H. *ICES J. Mar. Sci.* **1972,** *34*, 516. doi: 10.1093/icesjms/34.3.516

(63) Gao, X.; Wen, Y. J.; Qu, D.; An, L.; Luan, S. L.; Jiang, W. S.; Zong, X. P.; Liu, X. Y.; Sun, Z. C. *ACS Sustain. Chem. Eng.* **2018,** *6*, 5342. doi: 10.1021/acssuschemeng.8b00110

(64) Chen, R.; Yang, C. J.; Cai, W. Z.; Wang, H. Y.; Miao, J. W.; Zhang, L. P.; Chen, S. L.; Liu, B. *ACS Energy Lett.* **2017,** *2*, 1070. doi: 10.1021/acsenergylett.7b00219

(65) Yuen, S.; Pollard, A. *J. Sci. Food Agric.* **1952,** *3*, 441. doi: 10.1002/jsfa.2740031002

(66) Thompson, J.; Morrison, G. *Anal. Chem.* **1951,** *23*, 1153. doi: 10.1021/ac60056a029

(67) Searle, P. *Analyst* **1984,** *109*, 549. doi: 10.1039/an9840900549

(68) Michalski, R. *Separations* **2018,** *5*, 16. doi: 10.3390/separations5010016

(69) Butt, S. B.; Riaz, M. *J. Liq. Chromatogr. Relat. Technol.* **2009,** *32*, 1045. doi: 10.1080/10826070902841299

(70) Zhu, M.; Sun, Z.; Fujitsuka, M.; Majima, T. *Angew. Chem. Int. Ed.*

2018, *57*, 2160. doi: 10.1002/anie.201711357

(71) Shinde, S.; Bhosale, C.; Rajpure, K. *Catal. Rev.* **2013,** *55*, 79. doi: 10.1080/01614940.2012.734202

(72) Gligorovski, S.; Strekowski, R.; Barbati, S.; Vione, D. *Chem. Rev.* **2015,** *115*, 13051. doi: 10.1021/cr500310b

(73) Fu, Y. H.; Liang, W.; Guo, J. Q.; Tang, H.; Liu, S. S. *Appl. Surf. Sci.* **2018,** *430*, 234. doi: 10.1016/j.apsusc.2017.08.042

(74) Bao, Y. C.; Chen, K. Z. *Appl. Surf. Sci.* **2018,** *437*, 51. doi: 10.1016/j.apsusc.2017.12.075

(75) Chai, B.; Liu, C.; Yan, J.; Ren, Z.; Wang, Z. J. *Appl. Surf. Sci.* **2018,** *448*, 1. doi: 10.1016/j.apsusc.2018.04.116

(76) Che, H. N.; Liu, C. B.; Hu, W.; Hu, H.; Li, J. Q.; Dou, J. Y.; Shi, W. D.; Li, C. M.; Dong, H. J. *Catal. Sci. Technol.* **2018,** *8*, 622. doi: 10.1039/C7CY01709J

(77) Sun, M.; Wang, Y.; Shao, Y.; He, Y. H.; Zeng, Q.; Liang, H. K.; Yan, T.; Du, B. *J. Colloid Interface Sci.* **2017,** *501*, 123. doi: 10.1016/j.jcis.2017.04.047

(78) Wu, Y.; Wang, H.; Tu, W. G.; Liu, Y.; Tan, Y. Z.; Yuan, X. Z.; Chew, J. W. *J. Hazard Mater.* **2018,** *347*, 412. doi: 10.1016/j.jhazmat.2018.01.025

(79) Wu, Y.; Wang, H.; Tu, W. G.; Liu, Y.; Wu, S. Y.; Tan, Z. Y.; Chew, J. W. *Appl. Catal. B: Environ.* **2018,** *233*, 58. doi: 10.1016/j.apcatb.2018.03.105

(80) Yang, Y.; Wu, J. J.; Xiao, T. T.; Tang, Z.; Shen, J. Y.; Li, H.; Zhou, Y.; Zou, Z. G. *Appl. Catal. B: Environ.* **2019,** *255*, 117771. doi: 10.1016/j.apcatb.2019.117771

(81) Wang, S.; Zhu, B. C.; Liu, M. J.; Zhang, L. Y.; Yu, J. G.; Zhou, M. H. *Appl. Catal. B: Environ.* **2019,** *243*, 19. doi: 10.1016/j.apcatb.2018.10.019

(82) Zhang, M.; Lu, M.; Lang, Z. L.; Liu, J.; Liu, M.; Chang, J. N.; Li, L. Y.; Shang, L. J.; Wang, M.; Li, S. L.; *et al*. *Angew. Chem. Int. Ed.* **2020,** *132*, 6562. doi: 10.1002/anie.202000929

(83) Low, J. X.; Dai, B. Z.; Tong, T.; Jiang, C. J.; Yu, J. G. *Adv. Mater.* **2019,** *31*, 1802981. doi: 10.1002/adma.201802981

(84) He, Y. M.; Zhang, L. H.; Fan, M. H.; Wang, X. X.; Walbridge, M. L.; Nong, Q. Y.; Wu, Y.; Zhao, L. H. *Sol. Energy Mater Sol. Cells* **2015,** *137*, 175. doi: 10.1016/j.solmat.2015.01.037

(85) Ma, X. G.; Chen, C.; Hu, J. S.; Zheng, M. K.; Wang, H. H.; Dong, S. J.; Huang, C. Y.; Chen, X. B. *J. Alloy. Compd.* **2019,** *788*, 1. doi: 10.1016/j.jallcom.2019.02.044

(86) Zhu, B. C.; Zhang, L. Y.; Cheng, B.; Yu, J. G. *Appl. Catal. B: Environ.* **2018,** *224*, 983. doi: 10.1016/j.apcatb.2017.11.025

(87) Liu, J. J.; Cheng, B.; Yu, J. G. *Phys. Chem. Chem. Phys.* **2016,** *18*, 31175. doi: 10.1039/C6CP06147H

(88) Xu, D. F.; Cheng, B.; Wang, W. K.; Jiang, C. J.; Yu, J. G. *Appl. Catal. B: Environ.* **2018,** *231*, 368. doi: 10.1016/j.apcatb.2018.03.036

(89) Li, Z. W.; Hou, J. G.; Zhang, B.; Cao, S. Y.; Wu, Y. Z.; Gao, Z. M.; Nie, X. W.; Sun, L. C. *Nano Energy* **2019,** *59*, 537. doi: 10.1016/j.nanoen.2019.03.004

(90) Opoku, F.; Govender, K.; van Sittert, C.; Govender, P. *Appl. Surf. Sci.* **2018,** *427*, 487. doi: 10.1016/j.apsusc.2017.09.019

(91) Fu, C. F.; Zhang, R. Q.; Luo, Q. Q.; Li, X. X.; Yang, J. L. *J. Comput. Chem.* **2019,** *40*, 980. doi: 10.1002/jcc.25540

(92) Huang, Z. F.; Song, J. J.; Wang, X.; Pan, L.; Li, K.; Zhang, X. W.; Wang, L.; Zou, J. J. *Nano Energy* **2017,** *40*, 308. doi: 10.1016/j.nanoen.2017.08.032

(93) Zhang, J. F.; Fu, J. W.; Wang, Z. L.; Cheng, B.; Dai, K.; Ho, W. K. *J. Alloy. Compd.* **2018,** *766*, 841. doi: 10.1016/j.jallcom.2018.07.041

(94) Tong, T.; He, B.; Zhu, B. C.; Cheng, B.; Zhang, L. Y. *Appl. Surf. Sci.* **2018,** *459*, 385. doi: 10.1016/j.apsusc.2018.08.007

(95) Huang, Z.; Sun, Q.; Lv, K.; Zhang, Z. H.; Li, M.; Li, B. *Appl. Catal. B: Environ.* **2015,** *164*, 420. doi: 10.1016/j.apcatb.2014.09.043

(96) Yu, W. L.; Xu, D.; Peng, T. Y. *J. Mater. Chem. A* **2015,** *3*, 19936. doi: 10.1039/C5TA05503B

(97) Yu, W. L.; Chen, J.; Shang, T.; Chen, L.; Gu, L.; Peng, T. Y. *Appl. Catal. B: Environ.* **2017,** *219*, 693. doi: 10.1016/j.apcatb.2017.08.018

(98) Zhang, J. F.; Zhou, P.; Liu, J. J.; Yu, J. G. *Phys. Chem. Chem. Phys.* **2014,** *16*, 20382. doi: 10.1039/C4CP02201G

(99) Rudenko, A.; Brener, S.; Katsnelson, M. *Phys. Rev. Lett.* **2016,** *116*, 246401. doi: 10.1103/PhysRevLett.116.246401

(100) Miyata, A.; Mitioglu, A.; Plochocka, P.; Portugall, O.; Wang, J.; Stranks, S.; Snaith, H.; Nicholas, R. *Nat. Phys.* **2015,** *11*, 582. doi: 10.1038/NPHYS3357

(101) Wang, P.; Mao, Y.; Li, L.; Shen, Z.; Luo, X.; Wu, K.; An, P.; Wang, H.; Su, L.; Li, Y.; *et al*. *Angew. Chem. Int. Ed.* **2019,** *58*, 11329. doi: 10.1002/anie.201904571

(102) Chen, J. F.; Hu, C.; Deng, Z.; Gong, X. P.; Su, Y.; Yang, Q.; Zhong, J. B.; Li, J. Z.; Duan, R. *Chem. Phys. Lett.* **2019,** *716*, 134. doi: 10.1016/j.cplett.2018.12.026

(103) Maeda, K. *ACS Catal.* **2013,** *3*, 1486. doi: 10.1021/cs4002089

(104) Xu, F. Y.; Zhang, L. Y.; Cheng, B.; Yu, J. G. *ACS Sustain. Chem. Eng.* **2018,** *6*, 1229. doi: 10.1021/acssuschemeng.8b02710

(105) Zhang, S.; Wang, J. M.; Chen, S. T.; Li, R. J.; Peng, T. Y. *Ind. Eng. Chem. Res.* **2019,** *58*, 14802. doi: 10.1021/acs.iecr.9b02335

(106) Li, X. B.; Tung, C. H.; Wu, L. Z. *Angew. Chem. Int. Ed.* **2019,** *58*, 10804. doi: 10.1002/anie.201901267

(107) Guo, H.; Du, H.; Jiang, Y.; Jiang, N.; Shen, C. C.; Zhou, X.; Liu, Y. N.; Xu, A. W. *J. Phys. Chem. C* **2017,** *121*, 107. doi: 10.1021/acs.jpcc.6b10013

(108) Xu, Q. L.; Zhang, L. Y.; Cheng, B.; Fan, J. J.; Yu, J. G. *Chem* **2020,**

6, 1543. doi: 10.1016/j.chempr.2020.06.010

(109) Zeng, C.; Hu, Y.; Zhang, T.; Dong, F.; Zhang, Y. H.; Huang, H. W. *J. Mater. Chem. A* **2018,** *6*, 16932. doi: 10.1039/C8TA04258F

(110) Chao, Y.; Zhou, P.; Li, N.; Lai, J.; Yang, Y.; Zhang, Y. L.; Tang, Y. H.; Yang, W. X.; Du, Y. P.; Su, D.; *et al. Adv. Mater.* **2018,** *31*, 1807226. doi: 10.1002/adma.201807226

(111) Cui, H. J.; Li, B. B.; Li, Z. Y.; Li, X. Z.; Xu, S. *Appl. Surf. Sci.* **2018,** *455*, 831. doi: 10.1016/j.apsusc.2018.06.054

(112) Ma, K.; Yehezkeli, O.; Domaille, D.; Funke, H. H.; Cha, J. N. *Angew. Chem. Int. Ed.* **2015,** *54*, 11490. doi: 10.1002/anie.201504155

(113) Yuan, Q.C.; Liu, D.; Zhang, N.; Ye, W.; Ju, H. X.; Shi, L.; Long, R.; Zhu, J. F.; Xiong, Y. J. *Angew. Chem. Int. Ed.* **2017,** *15*, 4206. doi: 10.1002/anie.201700150

(114) Li, Y.; Li, L.; Gong, Y.; Bai, S.; Ju, H.; Wang, C.; Zhu, J. F.; Jiang, J.; Xiong, Y. J. *Nano Res.* **2015,** *8*, 3621. doi: 10.1007/s12274-015-0862-3

(115) Zhao, H.; Wu, M.; Liu, J.; Deng, Z.; Deng, Z.; Li, Y.; Su, B. L. *Appl. Catal. B: Environ.* **2016,** *184*, 182. doi: 10.1016/j.apcatb.2015.11.018

(116) Zhao, J.; Zhang, P.; Wang, Z.; Zhang, S.; Gao, H.; Hu, J. H.; Shao, G. S. *Sci. Rep.* **2017,** *7*, 16116. doi: 10.1038/s41598-017-12203-y

(117) Tahira, M.; Sirajb, M.; Tahira, B.; Umera, M.; Alias, H.; Othman, N. *Appl. Surf. Sci.* **2020,** *503*, 144344. doi: 10.1016/j.apsusc.2019.144344

(118) Liu, F.; Shi, R.; Wang, Z.; Weng, Y.; Che, C. M.; Chen, Y. *Angew. Chem. Int. Ed.* **2019,** *131*, 11917. doi: 10.1002/anie.201906416

(119) Wang, Q.; Hisatomi, T.; Suzuki, Y.; Pan, Z. J.; Seo, J.; Katayama, M.; Minegishi, T.; Nishiyama, H.; Takata, T.; Seki, K.; *et al. J. Am. Chem. Soc.* **2017,** *139*, 1675. doi: 10.1021/jacs.6b12164

(120) Iwase, A.; Yoshino, S.; Takayama, T.; Ng, Y.; Amal, R.; Kudo, A. *J. Am. Chem. Soc.* **2016,** *138*, 10260. doi: 10.1021/jacs.6b05304

(121) Chen, S. S.; Qi, Y.; Hisatomi, T.; Ding, Q.; Asai, T.; Li, Z.; Ma, S. S. K.; Zhang, F. X.; Domen, K.; Li, C. *Angew. Chem. Int. Ed.* **2015,** *54*, 8498. doi: 10.1002/anie.201502686

(122) Yuan, Y.; Chen, D.; Yang, S.; Yang, L.; Wang, J. J.; Cao, D. P.; Tu, W. G.; Yu, Z. T.; Zou, Z. G. *J. Mater. Chem. A* **2017,** *5*, 21205. doi: 10.1039/C7TA06644A

(123) Qi, Y.; Zhao, Y.; Gao, Y.; Li, D.; Li, Z.; Zhang, F. X.; Li, C. *Joule* **2018,** *2*, 2393. doi: 10.1016/j.joule.2018.07.029

(124) Wang, Q.; Hisatomi, T.; Jia, Q.; Tokudome, H.; Zhong, M.; Wang, C.; Pan, Z.; Takata, T.; Nakabayashi, M.; Shibata, N.; *et al. Nat. Mater.* **2016,** *15*, 611. doi: 10.1038/NMAT4589

(125) Wang, L.; Zheng, X.; Chen, L.; Xiong, Y.; Xu, H. *Angew. Chem. Int. Ed.* **2018,** *57*, 3454. doi: 10.1002/anie.201710557

(126) Yang, G.; Ding, H.; Che, D. M.; Feng, J. J.; Hao, Q.; Zhu, Y. F. *Appl. Catal. B: Environ.* **2018,** *234*, 260. doi: 10.1016/j.apcatb.2018.04.038

(127) Yoshino, S.; Iwase, A.; Ng, Y.; Amal, R.; Kudo, A. *ACS Appl. Energy Mater.* **2020,** *3*, 5684. doi: 10.1021/acsaem.0c00661

(128) Li, P.; Zhou, Y.; Li, H. J.; Xu, Q. F.; Meng, X. G.; Wang, X. Y.; Xiao, M.; Zou, Z. G. *Chem. Commun.* **2015,** *51*, 800. doi: 10.1039/c4cc08744e

(129) Kuai, L.; Zhou, Y.; Tu, W.; Li, P.; Li, H. J.; Xu, Q. F.; Tang, L. Q.; Wang, X. Y.; Xiao, M.; Zou, Z. G. *RSC Adv.* **2015,** *5*, 88409. doi: 10.1039/C5RA14374H

(130) Wang, J. C.; Zhang, L.; Fang, W. X.; Ren, J.; Li, Y. Y.; Yao, H. C.; Wang, J. S.; Li, Z. J. *ACS Appl. Mater. Interfaces.* **2015,** *7*, 8631. doi: 10.1021/acsami.5b00822

(131) Wang, Y.; Zhang, Z. Z.; Zhang, L. N.; Luo, Z. B.; Shen, J. N.; Lin, H. L.; Long, J.; Wu, J. C. S.; Fu, X. Z.; Wang, X. X; *et al. J. Am. Chem. Soc.* **2018,** *140*, 14595. doi: 10.1021/jacs.8b09344

(132) Shi, W.; Guo, X.; Cui, C.; Jiang, K.; Li, Z. J.; Qu, L. B.; Wang, J. C. *Appl. Catal. B: Environ.* **2019,** *243*, 236. doi: 10.1016/j.apcatb.2018.09.076

(133) Li, H. J.; Gao, Y. Y.; Zhou, Y.; Fan, F. T.; Han, Q. T.; Xu, Q. F.; Wang, X. Y.; Xiao, M.; Li, C.; Zou, Z. G. *Nano Lett.* **2016,** *16*, 5547. doi: 10.1021/acs.nanolett.6b02094

(134) Kim, C.; Cho, K. M.; Al-Saggaf, A.; Gereige, I.; Jung, H. *ACS Catal.* **2018,** *8*, 4170. doi: 10.1021/acscatal.7b03884

(135) Raza, A.; Shen, H.; Haidry, A.; Sun, L.; Liu, R.; Cui, S. *J. CO_2 Util.* **2020,** *37*, 260. doi: 10.1016/j.jcou.2019.12.020

(136) Zhou, R.; Wei, Z.; Li, Y.; Li, Z.; Yao, H. C. *J. Mater. Res.* **2019,** *34*, 3907. doi: 10.1557/jmr.2019.354

(137) Yanga, G.; Chena, D.; Ding, H.; Feng, J. J.; Zhang, J.; Zhu, Y. F.; Hamid, S.; Bahnemann, D. *Appl. Catal. B: Environ.* **2017,** *219*, 611. doi: 10.1016/j.apcatb.2017.08.016

(138) Aguirre, M.; Zhou, R.; Eugene, A.; Guzman, M.; Grela, M. *Appl. Catal. B: Environ.* **2017,** *217*, 485. doi: 10.1016/j.apcatb.2017.05.058

(139) Rong, X.; Chen, H.; Rong, J.; Zhang, X. Y.; Wei, J.; Liu, S.; Zhou, X. T.; Xu, J. C.; Qiu, F. X.; Wu, Z. R. *Chem. Eng. J.* **2019,** *371*, 286. doi: 10.1016/j.cej.2019.04.052

(140) Xu, Q. L.; Zhang, L. Y.; Yu, J. G.; Wageh, S.; Al-Ghamdi, A.; Jaroniec, M. *Mater. Today* **2018,** *21*, 1042. doi: 10.1016/j.mattod.2018.04.008

(141) Di, T. M.; Xu, Q. L.; Ho, W. K.; Tang, H.; Xiang, Q. J.; Yu, J. G. *ChemCatChem* **2019,** *11*, 1394. doi: 10.1002/cctc.201802024

(142) Xu, F. Y.; Zhang, L. Y.; Cheng, B.; Yu, J. G. *ACS Sustain. Chem. Eng.* **2018,** *6*, 12291. doi: 10.1021/acssuschemeng.8b02710

(143) Meng, A. Y.; Zhu, B. C.; Zhong, B.; Zhang, L. Y.; Cheng, B. *Appl. Surf. Sci.* **2017,** *422*, 518. doi: 10.1016/j.apsusc.2017.06.028

(144) Jin, J.; Yu, J. G.; Guo, D. P.; Cui, C.; Ho, W. K. *Small* **2015,** *11*, 5262. doi: 10.1002/smll.201500926

(145) Cao, D.; An, H.; Yan, X. Q.; Zhao, Y. X.; Yang, G. D.; Mei, H. *Acta Phys. -Chim. Sin.* **2020,** *36*, 1901051. [曹丹, 安华, 严孝清, 赵宇鑫, 杨贵东, 梅辉. 物理化学学报, **2020,** *36*, 1901051.] doi: 10.3866/PKU.WHXB201901051

(146) Xu, D. F.; Cheng, B.; Cao, S. W.; Yu, J. G. *Appl. Catal. B: Environ.* **2015,** *164*, 380. doi: 10.1016/j.apcatb.2014.09.051

(147) Zhou, P.; Yu, J. G.; Jaroniec, M. *Adv. Mater.* **2014,** *26*, 4920. doi: 10.1002/adma.201400288

(148) Jiang, T. G.; Wang, K.; Guo, T.; Wu, X. Y.; Zhang, G. K. *Chin. J. Catal.* **2020,** *41*, 161. doi: 10.1016/S1872-2067(19)63391-7

(149) Li, Z.; Wang, X.; Zhang, J. F.; Liang, C. H.; Lu, L. H.; Dai, K. *Chin. J. Catal.* **2019,** *40*, 326. doi: 10.1016/S1872-2067(18)63165-1

(150) Wang, J. M.; Kuo, M. D.; Zeng, P.; Xu, L.; Chen, S. T.; Peng, T. Y. *Appl. Catal. B: Environ.* **2020,** *279*, 119377. doi: 10.1016/j.apcatb.2020.119377

(151) Zhang, S.; Chen, S. T.; Liu, D.; Zhang, J.; Peng, T. Y. *Appl. Surf. Sci.* **2020,** *529*, 147013. doi: 10.1016/j.apsusc.2020.147013

(152) Muraoka, K.; Uchiyama, T.; Lu, D.; Uchimoto, Y.; Ishitani, O.; Maeda, K. *Bull. Chem. Soc. Jpn.* **2019,** *92*, 124. doi: 10.1246/bcsj.20180239

(153) Nie, N.; He, F.; Zhang, L. Y.; Cheng, B. *Appl. Surf. Sci.* **2018,** *457*, 1096. doi: 10.1016/j.apsusc.2018.07.002

(154) Ran, J. R.; Zhang, J.; Yu, J. G.; Jaroniec, M.; Qiao, S. *Chem. Soc. Rev.* **2014,** *43*, 7787. doi: 10.1039/C3CS60425J

(155) Kudo, A.; Miseki, Y. *Chem. Soc. Rev.* **2009,** *38*, 253. doi: 10.1039/B800489G

(156) Xi, G. C.; Ouyang, S. X.; Li, P.; Ye, J. H.; Ma, Q.; Su, N.; Bai, H.; Wang, C. *Angew. Chem. Int. Ed.* **2012,** *51*, 2395. doi: 10.1002/anie.201107681

(157) Polleux, J.; Pinna, N.; Antonietti, M.; Niederberger, M. *J. Am. Chem. Soc.* **2005,** *127*, 15595. doi: 10.1021/ja0544915

(158) Kailasam, K.; Fischer, A.; Zhang, G.; Zhang, J.; Schwarze, M.; Schrçder, M.; Wang, X. C.; Schomäcker, R.; Thomas, A. *ChemSusChem* **2015,** *8*, 1404. doi: 10.1002/cssc.201403278

(159) Chen, S. F.; Hu, Y. F.; Jiang, X. L.; Meng, S. G.; Fu, X. L. *Mater. Chem. Phys.* **2015,** *149*. 512. doi: 10.1016/j.matchemphys.2014.11.001

(160) Cao, S. W.; Low, J. X.; Yu, J. G.; Jaroniec, M. *Adv. Mater.* **2015,** *27*, 2150. doi: 10.1002/adma.201500033

(161) Zhang, Z. Y.; Huang, J. D.; Fang, Y. R.; Zhang, M. Y.; Liu, K. C.; Dong, B. *Adv. Mater.* **2017,** *29*, 1606688. doi: 10.1002/adma.201606688

(162) Wang, X.; Liow, C.; Bisht, A.; Liu, X.; Sum, T. C.; Chen, X. S; Li, S. Z. *Adv. Mater.* **2015,** *27*, 2207. doi: 10.1002/adma.201405674

(163) Zhang, Z. Y.; Liu, K. C.; Feng, Z. Q.; Bao, Y. N.; Dong, B. *Sci. Rep.* **2016,** *6*, 19221. doi: 10.1038/srep19221

(164) Pachfule, P.; Acharjya, A.; Roeser, J.; Langenhahn, T.; Schwarze, M.; Schomacker, R.; Thomas, A.; Schmidt, J. *J. Am. Chem. Soc.* **2018,** *140*, 1423. doi: 10.1021/jacs.7b11255

(165) Jin, E.; Lan, Z.; Jiang, Q.; Geng, K.; Li, G.; Wang, X.; Jiang, D. *Chem* **2019,** *5*, 1632. doi: 10.1039/C9TA12870K

(166) Banerjee, T.; Haase, F.; Savasci, G.; Gottschling, K.; Ochsenfeld, C.; Lotsch, B. V. *J. Am. Chem. Soc.* **2017,** *139*, 16228. doi: 10.1021/jacs.7b07489

(167) Dong, Z.; Wu, Y.; Thirugnanam, N.; Li, G. *Appl. Surf. Sci.* **2018,** *430*, 293. doi: 10.1016/j.apsusc.2017.07.186

(168) Kong, L. N.; Zhang, X. T.; Wang, C. H.; Xu, J. P.; Du, X. W.; Li, L. *Appl. Surf. Sci.* **2018,** *448*, 288. doi: 10.1016/j.apsusc.2018.04.011

(169) Qin, Z.; Fang, W. J.; Liu, J. Y.; Wei, Z.; Jiang, Z.; Shangguan, W. F. *Chin. J. Catal.* **2018,** *39*, 472. doi: 10.1016/S1872-2067(17)62961-9

(170) Hagiwara, H.; Watanabe, M.; Ida, S.; Ishihara, T. *J. Jpn. Pet. Inst.* **2017,** *60*, 10. doi: 10.1627/jpi.60.10

(171) Bai, Y.; Nakagawa, K.; Cowan, A.; Aitchison, C.; Yamaguchi, Y.; Zwijnenburg, M.; Kudo, A.; Sprick, R.; Cooper, A. I. *J. Mater. Chem. A* **2020,** *8*, 16283. doi: 10.1039/D0TA04754F

(172) Kuehnel, M.; Orchard, K.; Dalle, K.; Reisner, E. *J. Am. Chem. Soc.* **2017,** *139*, 7217. doi: 10.1021/jacs.7b00369

(173) Ryu, A. *Chem. Soc. Jpn.* **2011,** *84*, 1000. doi: 10.1246/bcsj.20110132

(174) Suzuki, T.; Yoshino, S.; Takayama, T.; Iwase, A.; Kudo, A.; Morikawa, T. *Chem. Commun.* **2018,** *54*, 10199. doi: 10.1039/C8CC05505J

(175) Liao, M.; Scheiner, S. *J. Chem. Phys.* **2002,** *117*, 205. doi: 10.1063/1.1480872

(176) Dong, Y.; Li, J.; Shi, L.; Guo, Z. G. *ACS Appl. Mater. Interfaces* **2015,** *7*, 15403. doi: 10.1021/acsami.5b03486

(177) Choi, S.; Yang, H.; Kim, J.; Park, H. *Appl. Catal. B: Environ.* **2012,** *121*, 206. doi: 10.1016/j.apcatb.2012.04.011

(178) Zhang, N.; Yang, M. Q.; Liu, S. Q.; Sun, Y. G.; Xu, Y. J. *Chem. Rev.* **2015,** *115*, 10307. doi: 10.1021/acs.chemrev.5b00267

(179) Wibmer, L.; Lourenco, L.; Roth, A.; Katsukis, G.; Neves, M.; Cavaleiro, J.; Torres, T.; Guldi, D. *Nanoscale* **2015,** *7*, 5674. doi: 10.1039/C4NR05719H

(180) Bai, Y.; Ye, L.; Wang, L.; Shi, X.; Wang, P.; Bai, W.; Wong, P. K. *Appl. Catal. B: Environ.* **2016,** *194*, 98. doi: 10.1016/j.apcatb.2016.04.052

(181) Meng, J. C.; Chen, Q.; Lu, J. Q.; Liu, H. *ACS Appl. Mater. Interfaces* **2019,** *11*, 550. doi: 10.1021/acsami.8b14282

(182) Wang, L.; Jin, P.; Huang, J.; She, H.; Wang, Q. *ACS Sustain. Chem.*

Eng. **2019,** *7*, 15660. doi: 10.1021/acssuschemeng.7b01970

(183) Bian, J.; Feng, J. N.; Zhang, Z. Q.; Sun, J. W.; Chu, M. N.; Sun, L.; Li, X.; Tang, D. Y.; Jing, L. Q. *Chem. Commun.* **2020,** *56*, 4926. doi: 10.1039/D0CC01518K

(184) Xu, F. Y.; Meng, K.; Cheng, B.; Wang, S. Y.; Xu, J. S.; Yu, J. G. *Nat. Commun.* **2020,** *11*, 4613. doi: 10.1038/s41467-020-18350-7

(185) He, Y. M.; Zhang, L. H.; Teng, B. T.; Fan, M. H. *Environ. Sci. Technol.* **2015,** *49*, 649. doi: 10.1021/es5046309

(186) Bai, Y.; Chen, T.; Wang, P. Q.; Wang, L.; Ye, L. Q; Shi, X.; Bai, W. *Sol. Energy Mater. Sol. Cells* **2016,** *157*, 406. doi: 10.1016/j.solmat.2016.07.001

(187) Wu, J.; Feng, Y. J.; Bruce, L.; Dai, C. C.; Han, X. Y.; Li, D.; Liu, J. *ACS Sustain. Chem. Eng.* **2019,** *7*, 15289. doi: 10.1021/acssuschemeng.9b02489

(188) Jing, X.; He, C.; Yang, Y.; Duan, C. Y. *J. Am. Chem. Soc.* **2015,** *137*, 3967. doi: 10.1021/jacs.5b00832

(189) Asahi, R.; Morikawa, T.; Ohwaki, T.; Aoki, K.; Taga, Y. *Science* **2001,** *293*, 269. doi: 10.1126/science.1061051

(190) Li, X.; Kikugawa, N.; Ye, J. *Adv. Mater.* **2008,** *20*, 3816. doi: 10.1002/adma.200702975

(191) Oshima, T.; Nishioka, S.; Kikuchi, Y.; Hirai, S.; Yanagisawa, K.; Eguchi, M.; Miseki, Y.; Yokoi, T.; Yui, T.; Kimoto, K.; *et al. J. Am. Chem. Soc.* **2020,** *142*, 8412. doi: 10.1021/jacs.0c02053

(192) Gerischer, H. *Photochem. Photobiol.* **1972,** *16*, 243. doi: 10.1111/j.1751-1097.1972.tb06296.x

(193) Bae, E.; Choi, W.; Park, J.; Shin, H.; Kim, S.; Lee, J. *J. Phys. Chem. B* **2004,** *108*, 14093. doi: 10.1021/jp047777p

(194) Linic, S.; Christopher, P.; Ingram, D. B. *Nat. Mater.* **2011,** *10*, 911. doi: 10.1038/NMAT3151

(195) Tatsuma, T.; Nishi, H.; Ishida, T. *Chem. Sci.* **2017,** *8*, 3325. doi: 10.1039/C7SC00031F

(196) Zhou, H.; Long, J.; Yaghi, O. *Chem. Rev.* **2017,** *112*, 673. doi: 10.1021/cr300014x

(197) Gao, S.; Lin, Y.; Jiao, X. C.; Sun, Y. F.; Luo, Q. Q.; Zhang, W. H.; Li, D. Q.; Yang, J. L.; Xie, Y. *Nature* **2016,** *529*, 68. doi: 10.1038/nature16455

(198) Gao, C.; Wang, J.; Xu, H. X.; Xiong, Y. J. *Chem. Soc. Rev.* **2017,** *46*, 2799. doi: 10.1039/C6CS00727A

(199) Luo, B.; Liu, G.; Wang, L. Z. *Nanoscale* **2016,** *8*, 6904. doi: 10.1039/C6NR00546B

(200) She, X.; Wu, J.; Xu, H.; Zhong, J.; Wang, Y.; Song, Y. H.; Nie, K. Q.; Liu, Y.; Yang, Y. C.; Rodrigues, M.; *et al. Adv. Energy Mater.* **2017,** *7*, 1700025. doi: 10.1002/aenm.201700025

(201) Chiarello, G.; Dozzi, M.; Scavini, M.; Grunwaldt, J.; Selli, E. *Appl. Catal. B: Environ.* **2014,** *160/161*, 144. doi: 10.1016/j.apcatb.2014.05.006

(202) Ye, S.; Ding, C. M.; Liu, M. Y.; Wang, A. Q.; Huang, Q. G.; Li, C. *Adv. Mater.* **2019,** *31*, 1902069. doi: 10.1002/adma.201902069

(203) Luo, W. J.; Jiang, C. R.; Li, Y. M.; Shevlin, S.; Han, X. Y.; Qiu, K. P.; Cheng, Y. C.; Guo, Z. X.; Huang, W.; Tang, J. W. *J. Mater. Chem. A* **2017,** *5*, 2021. doi: 10.1039/C6TA08719A

(204) Yang, J. H.; Wang, D. E.; Han, H. X.; Li, C. *Acc. Chem. Res.* **2013,** *46*, 1900. doi: 10.1021/ar300227e

(205) Maeda, K.; Teramura, K.; Lu, D.; Saito, N.; Inoue, Y.; Domen, K. *Angew. Chem. Int. Ed.* **2006,** *45*, 7806. doi: 10.1002/anie.200602473

(206) Yoshida, M.; Takanabe, K.; Maeda, K.; Ishikawa, A.; Kubota, J.; Sakata, Y.; Ikezawa, Y.; Domen, K. *J. Phys. Chem. C* **2009,** *113*, 10151. doi: 10.1021/jp901418u

(207) Zhu, M. S.; Kim, S.; Mao, L.; Fujitsuka, M.; Zhang, J. Y.; Wang, X. C.; Majima, T. *J. Am. Chem. Soc.* **2017,** *139*, 13234. doi: 10.1021/jacs.7b08416

(208) Zhu, M.; Zhai, C.; Fujitsuka, M.; Majima, T. *Appl. Catal. B: Environ.* **2018,** *221*, 645. doi: 10.1016/j.apcatb.2017.09.063

(209) Martin, D.; Reardon, P.; Moniz, S.; Tang, J. *J. Am. Chem. Soc.* **2014,** *136*, 12568. doi: 10.1021/ja506386e

(210) Nie, Z. H.; Wang, Y. H.; Li, Z. L.; Sun, Y.; Qin, S. C.; Liu, X. P.; Turcu, I. C. E.; Shi, Y.; Zhang, R.; Ye, Y.; *et al. Nanoscale Horiz.* **2019,** *4*, 1099. doi: 10.1039/c9nh00045c

(211) Du, Y.; Wang, Z.; Chen, H.; Wang, H. Y.; Liu, G.; Weng, Y. *Phys. Chem. Chem. Phys.* **2019,** *21*, 4349. doi: 10.1039/C8CP06109B

(212) Zhu, M.; Sun, Z.; Fujitsuka, M.; Majima, T. *Angew. Chem. Int. Ed.* **2018,** *130*, 2182. doi: 10.1002/anie.201711357

(213) Sun, D.; Jang, S.; Yim, S. J.; Ye, L.; Kim, D. P. *Adv. Funct. Mater.* **2018,** *28*, 1707110. doi: 10.1002/adfm.201707110

(214) Liu, M.; Qiao, L. Z.; Dong, B. B.; Guo, S.; Yao, S.; Chao, L.; Zhang, Z. M.; Lu, T. B. *Appl. Catal. B: Environ.* **2020,** *273*, 119066. doi: 10.1016/j.apcatb.2020.119066

(215) Xu, F. Y.; Zhang, J. J.; Zhu, B. C.; Yu, J. G.; Xu, J. S. *Appl. Catal. B: Environ.* **2018,** *230*, 194. doi: 10.1016/j.apcatb.2018.02.042

(216) Qi, K. Z.; Cheng, B.; Yu, J. G.; Ho, W. *Chin. J. Catal.* **2017,** *38*, 1936. doi: 10.1016/S1872-2067(17)62962-0

(217) Zeng, D.; Zhou, T.; Ong, W.; Wu, M.; Duan, X.; Xu, W.; Chen, Y.; Zhu, Y.; Peng, D. *ACS Appl. Mater. Interfaces* **2019,** *11*, 5651. doi: 10.1021/acsami.5b10785

(218) Wan, Y.; Wang, L.; Xu, H.; Wu, X. J.; Yang, J. L. *J. Am. Chem. Soc.* **2020,** *142*, 4508. doi: 10.1021/jacs.0c00564

(219) Liu, Y.; Cui, J.; Liang, Y.; An, W. J.; Wang, H.; Liu, L.; Hu, J. S.; Cui, W. Q. *Appl. Surf. Sci.* **2020,** *509*, 145296. doi: 10.1016/j.apsusc.2020.145296

(220) Zhou, G.; Wu, M. F.; Xing, Q. J.; Li, F.; Liu, H.; Luo, X. B.; Zou, J. P.; Luo, J. M.; Zhang, A. Q. *Appl. Catal. B: Environ.* **2018,** *220*, 607. doi: 10.1016/j.apcatb.2017.08.086

(221) Zhang, X. H.; Peng, T. Y.; Song, S. S. *J. Mater. Chem. A* **2016,** *4*, 2365. doi: 10.1039/C5TA08939E

(222) Mathew, S.; Yella, A.; Gao, P.; Humphry-Baker, R.; Curchod, B.; Ashari-Astani, N.; Tavernelli, I.; Rothlisberger, U.; Nazeeruddin, M.; Gratzel, M. *Nat. Chem.* **2014,** *6*, 242. doi: 10.1038/NCHEM.1861

(223) Adán, C.; Magnet, A.; Fenoy, S.; Pablos, C.; del Águila, C.; Marugán, J. *Water Res.* **2018,** *144*, 512. doi: 10.1016/j.watres.2018.07.060

(224) Montes, V.; Pérez-Bolívar, C.; Agarwal, N.; Shinar, J.; Anzenbacher, P. *J. Am. Chem. Soc.* **2006,** *128*, 12436. doi: 10.1021/ja064471i

(225) Gu, C.; Huang, N.; Chen, Y. C.; Zhang, H. H.; Zhang, S. T.; Li, F. H.; Ma, Y. G.; Jiang, D. L. *Angew. Chem. Int. Ed.* **2016,** *128*, 3101. doi: 10.1002/anie.201510723

(226) Wang, Z.; Ghasimi, S.; Landfester, K.; Zhang, K. *Adv. Mater.* **2015,** *27*, 6265. doi: 10.1002/adma.201502735

(227) Zhang, Y. P.; Tang, H. L.; Dong, H.; Gao, M. Y.; Li, C. C.; Sun, X.; Wei, J.; Qu, Y.; Li, Z.; Zhang, F. M. *J. Mater. Chem. A* **2020,** *8*, 4334. doi: 10.1039/C9TA12870K

(228) Erbs, W.; Desilvestro, J.; Borgarello, E.; Graetzel, M. *J. Phys. Chem.* **1984,** *88*, 4001. doi: 10.1021/j150662a028

(229) Lou, Z. Z.; Gu, Q.; Xu, L.; Liao, Y. S.; Xue, C. *Chem. Asian J.* **2015,** *10*, 1291. doi: 10.1002/asia.201500319

(230) Yan, J. Q.; Wang, T.; Wu, G. J.; Dai, W. L.; Guan, N. J.; Li, L. D.; Gong, J. L. *Adv. Mater.* **2015,** *27*, 1580. doi: 10.1002/adma.201404792

(231) Liu, J.; Margeat, O.; Dachraoui, W.; Liu, X.; Fahlman, M.; Ackermann, J. *Adv. Funct. Mater.* **2014,** *24*, 6029. doi: 10.1002/adfm.201401261

(232) Hua, S.; Qu, D.; An, L.; Jiang, W.; Wen, Y.; Wang, X. Y.; Sun, Z. C. *Appl. Catal. B: Environ.* **2019,** *240*, 253. doi: 10.1016/j.apcatb.2018.09.010

(233) Jo, W.; Kumar, S.; Eslava, S.; Tonda, S. *Appl. Catal. B: Environ.* **2018,** *239*, 586. doi: 10.1016/j.apcatb.2018.08.056

(234) Dalapati, S.; Jin, S.; Gao, J.; Xu, Y.; Nagai, A.; Jiang, D. *J. Am. Chem. Soc.* **2013,** *135*, 17310. doi: 10.1021/ja4103293

(235) Zhou, L.; Kamyab, H.; Surendar, A.; Maseleno, A.; Ibatova, A. Z.; Chelliapan, S.; Karachi, N.; Parsaee, Z. *J. Photochem. Photobiol. A-Chem.* **2019,** *368*, 30. doi: 10.1016/j.jphotochem.2018.09.006

(236) Ong, W.; Tan, L.; Ng, Y.; Yong, S. T.; Chai, S. P. *Chem. Rev.* **2016,** *116*, 7159. doi: 10.1021/acs.chemrev.6b00075

(237) Di, T.; Zhu, B.; Cheng, B.; Yu, J. G.; Xu, J. S. *J. Catal.* **2017,** *352*, 532. doi: 10.1016/j.jcat.2017.06.006

(238) Hoffman, B.; Dean, D.; Seefeldt, L. *Acc. Chem. Res.* **2009,** *42*, 609. doi: 10.1021/ar8002128

(239) Kim, J.; Rees, D. C. *Biochemistry* **1994,** *33*, 389. doi: 10.1021/bi00168a001

(240) Brown, K. A.; Harris, D. F.; Wilker, M. B.; Rasmussen, A.; Khadka, N.; Hamby, H.; Keable, S.; Dukovic, G.; Peters, J. W.; Seefeldt, L. C.; King, P. W. *Science* **2016,** *352*, 448. doi: 10.1126/science.aaf2091

(241) Wang, Y. J.; Wei, W. S.; Li, M. Y.; Hu, S. Z.; Zhang, J.; Feng, R. J. *RSC Adv.* **2017,** *7*, 18099. doi: 10.1039/C7RA00097A

(242) Cao, S. H.; Zhou, N.; Gao, F. H.; Chen, H.; Jiang, F. *Appl. Catal. B: Environ.* **2017,** *218*, 600. doi: 10.1016/j.apcatb.2017.07.013

(243) Feng, X. W.; Chen, H.; Jiang, F.; Wang, X. *Catal. Sci. Technol.* **2019,** *9*, 2849. doi: 10.1039/C9CY00281B

(244) Yu, L. M.; Mo, Z.; Zhu, X. L.; Deng, J. J.; Xu, F.; Song, Y. H.; She, Y. B.; Li, H. M.; Xu, H. *Green Energy Environ.* **2020,** doi: 10.1016/j.gee.2020.05.011

(245) Liang, H. Y.; Zou, H.; Hu, S. Z. *New J. Chem.* **2017,** *41*, 8920. doi: 10.1039/C7NJ01848G

(246) Zhao, X.; You, Y.; Huang, S.; Wu, Y. X.; Ma, Y. Y.; Zhang, G.; Zhang, Z. H. *Appl. Catal. B: Environ.* **2020,** *278*, 119251. doi: 10.1016/j.apcatb.2020.119251

(247) Ding, L.; Zhou, H.; Lou, S.; Ding, J.; Zhang, D.; Zhu, H. X.; Fan, T. X. *Int. J. Hydrog. Energy* **2013,** *38*, 8244. doi: 10.1016/j.ijhydene.2013.04.093

(248) Li, Y. F.; Zhou, M. H.; Cheng, B.; Yan, S. *J. Mater. Sci. Technol.* **2020,** *56*, 1. doi: 10.1016/j.jmst.2020.04.028

(249) Pan, J. B; Shen, S.; Zhou, W.; Tang, J.; Ding, H. Z.; Wang, J. B.; Chen, L.; Au, C.; Yin, S. F. *Acta Phys. -Chim. Sin.* **2020,** *36*, 1905068. [潘金波, 申升, 周威, 唐杰, 丁洪志, 王进博, 陈浪, 区泽堂, 尹双凤. 物理化学学报, **2020,** *36*, 1905068.] doi: 10.3866/PKU.WHXB201905068

(250) Nie, N.; Zhang, L. Y.; Fu, J. W.; Cheng, B.; Yu, J. G. *Appl. Surf. Sci.* **2018,** *441*, 12. doi: 10.1016/j.apsusc.2018.01.193

(251) Xia, P. F.; Zhu, B. C.; Cheng, B.; Yu, J. G.; Xu, J. S. *ACS Sustain. Chem. Eng.* **2018,** *6*, 965. doi: 10.1021/acssuschemeng.7b03289

(252) Zhu, B. C.; Xia, P. F.; Li, Y.; Ho, W.; Yu, J. G. *Appl. Surf. Sci.* **2017,** *391*, 175. doi: 10.1016/j.apsusc.2016.07.104

(253) Li, X. B.; Xiong, J.; Xu, Y.; Feng, Z. J.; Huang, J. T. *Chin. J. Catal.* **2019,** *40*, 424. doi: 10.1016/S1872-2067(18)63183-3

(254) Hu, L. M.; Yan, J. T.; Wang, C. L.; Chai, B.; Li, J. F. *Chin. J. Catal.* **2019,** *40*, 458. doi: 10.1016/S1872-2067(18)63181-X

(255) Fang, M. M.; Shao, J. X.; Huang, X. G.; Wang, J. Y. *J. Mater. Sci. Technol.* **2020,** *56*, 133. doi: 10.1016/j.jmst.2020.01.054

(256) Yu, W. L.; Zhang, S.; Chen, J. X.; Xia, P. F.; Richter, M.; Chen, L. F.; Xu, W.; Jin, J. P.; Chen, S. L.; Peng, T. Y. *J. Mater. Chem. A* **2018,** *6*, 15668. doi: 10.1039/C8TA02922A

(257) Yuan, J. L.; Wen, J. Q.; Zhong, Y. M.; Li, X.; Fang, Y. P.; Zhang, S. S.; Liu, W. *J. Mater. Chem. A* **2015,** *3*, 18244. doi: 10.1039/C5TA04573H

(258) Liu, D.; Zhang, S.; Wang, J.; Peng, T. Y.; Li, R. J. *ACS Appl. Mater. Interfaces* **2019,** *11*, 27913. doi: 10.1021/acsami.9b08329

(259) Dong, J.; Shi, Y.; Huang, C. P.; Wu, Q.; Zeng, T.; Yao, W. F. *Appl. Catal. B: Environ.* **2019**, *243*, 27. doi: 10.1016/j.apcatb.2018.10.016

(260) Liu, Y. J.; Liu, H. X.; Zhou, H. M.; Li, T.; Zhang, L. N. *Appl. Surf. Sci.* **2019,** *466*, 133. doi: 10.1016/j.apsusc.2018.10.027

(261) Zhao, Y. S.; Fu, H. B.; Peng, A. D.; Ma, Y.; Liao, Q.; Yao, J. N. *Acc. Chem. Res*. 2**010,** *43*, 409. doi: 10.1021/ar900219n

(262) Fu, J. W.; Yu, J. G.; Jiang, C.; Cheng, B. *Adv. Energy Mater.* **2017,** *8*, 1701503. doi: 10.1002/aenm.201701503

(263) Liess, A.; Stolte, M.; He, T.; Würthner, F. *Dye. Mater. Horiz.* **2016,** *3*, 72. doi: 10.1039/C5MH00167F

(264) Ren, Y.; Sun, D.; Cao, Y.; Tsao, H.; Yuan, Y.; Zakeeruddin, S.; Wang, P.; Gratzel, M. *J. Am. Chem. Soc.* **2018,** *140*, 2405. doi: 10.1021/jacs.7b12348

(265) Gsanger, M.; Bialas, D.; Huang, L.; Stolte, M.; Würthner, F. *Adv. Mater.* **2016,** *28*, 3615. doi: 10.1002/adma.201505440

(266) Li, H. H.; Jie, L. L.; Pan, J.N.; Kang, L. T.; Yao, J. N. *J. Mater. Chem. A* **2016,** *4*, 6577. doi: 10.1039/C6TA01582D

(267) Liu, L. J.; Lai, Y. D.; Li, H. H.; Kang, L. T.; Liu, J. J.; Cao, Z. M.; Yao, J. N. *J. Mater. Chem. A* **2017,** *5*, 8029. doi: 10.1039/C7TA00580F

(268) Niishiro, R.; Kato, H.; Kudo, A. *Phys. Chem. Chem. Phys.* **2005,** *7*, 2241. doi: 10.1039/B502147B

(269) Sakata, Y.; Matsuda, Y.; Yanagida, T.; Hirata, K.; Imamura, H.; Teramura, K. *Catal. Lett.* **2008,** *125*, 22. doi: 10.1007/s10562-008-9557-7

(270) Yashima, M.; Lee, Y.; Domen, K. *Chem. Mater.* **2007,** *19*, 588. doi: 10.1021/cm062586f

(271) Liu, Q. X.; Zeng, C. M.; Ai, L. H.; Hao, Z.; Jiang, J. *Appl. Catal. B: Environ.* **2018,** *224*, 38. doi: 10.1016/j.apcatb.2017.10.029

(272) Pan, Z. M.; Liu, M. H.; Niu, P. P.; Guo, F. S.; Fu, X. Z.; Wang, X. C. *Acta Phys. -Chim. Sin.* **2020,** *36*, 1906014. [潘志明，刘明辉，牛萍萍，郭芳松，付贤智，王心晨. 物理化学学报，**2020,** *36*, 1906014.] doi: 10.3866/PKU.WHXB201906014

(273) Ran, J.; Jaroniec, M.; Qiao, S. *Adv. Mater.* **2018,** *30*, 1704649. doi: 10.1002/adma.201704649

(274) Xu, Q. L.; Zhu, B. C.; Jiang, C. J.; Cheng, B.; Yu, J. G. *Solar RRL.* **2018,** *2*, 1800006. doi: 10.1002/solr.201800006

(275) Nakada, A.; Kuriki, R.; Sekizawa, K.; Nishioka, S.; Vequizo, J.; Uchiyama, T.; Kawakami, N.; Lu, D. L.; Yamakata, A.; Uchimoto, Y.; *et al. ACS Catal.* **2018,** *8*, 9744. doi: 10.1021/acscatal.8b03062

(276) Wu, M.; Li, L.; Liu, N.; Wang, D. J.; Xue, Y. C.; Tang, L. *Process Safety Environ. Protect.* **2018,** *118*, 40. doi: 10.1016/j.psep.2018.06.025

(277) Shen, R. C.; Zhang, L. P.; Chen, X. Z.; Jaroniec, M.; Li, N.; Li, X. *Appl. Catal. B: Environ.* **2020,** *266*, 118619. doi: 10.1016/j.apcatb.2020.118619

(278) Shen, Z.; Yuan, Y.; Wang, P.; Bai, W. F.; Pei, L.; Wu, S. T.; Yu, Z. T.; Zou, Z. G. *ACS Appl. Mater. Interfaces* **2020,** *12*, 17343. doi: 10.1021/acsami.9b21167

(279) Miseki, Y.; Sayama, K. *RSC Adv.* **2014,** *4*, 8308. doi: 10.1039/C3RA47772J

(280) Miseki, Y.; Sayama, K. *Catal. Sci. Technol.* **2019,** *9*, 2019. doi: 10.1039/C9CY00100J

(281) Zhang, X.; Han, F.; Shi, B.; Farsinezhad, S.; Dechaine, G.; Shankar, K. *Angew. Chem. Int. Ed.* **2012,** *51*, 12732. doi: 10.1002/anie.201205619

(282) Liu, J. F.; Wang, P.; Fan, J. J.; Yu, H. G. *J. Energy Chem.* **2020,** *51*, 253. doi: 10.1016/j.jechem.2020.03.085

(283) Gao, D. D.; Yuan, R. R.; Fan, J. J.; Hong, X. K.; Yu, H. G. *J. Mater. Sci. Technol.* **2020,** *56*, 122. doi: 10.1016/j.jmst.2020.02.031

(284) Wang, L.; Zhu, C. G.; Yin, L. S.; Huang, W. *Acta Phys. -Chim. Sin.* **2020,** *36*, 1907001. [王梁，朱澄鹭，殷丽莎，黄维. 物理化学学报, **2020,** *36*, 1907001.] doi: 10.3866/PKU.WHXB201907001

(285) Iizuka, K.; Wato, T.; Miseki, Y.; Saito, K.; Kudo, A. *J. Am. Chem. Soc.* **2011,** *133*, 20863. doi: 10.1021/ja207586e

(286) Xie, S. J.; Wang, Y.; Zhang, Q. H.; Deng, W. P.; Wang, Y. *ACS Catal.* **2014,** *4*, 3644. doi: 10.1021/cs500648p

(287) Lin, H. Y.; Yang, H. C.; Wang, W. L. *Catal. Today* **2011,** *174*, 106. doi: 10.1016/j.cattod.2011.01.052

(288) Zhang, Z. Y.; Wang, Z.; Cao, S. W.; Xue, C. *J. Phys. Chem. C* **2013,** *117*, 25939. doi: 10.1021/jp409311x

(289) Wang, W.; An, W.; Ramalingam, B.; Mukherjee, S.; Niedzwiedzki, D.; Gangopadhyay, S.; Biswas, P. *J. Am. Chem. Soc.* **2012,** *134*, 11276. doi: 10.1021/ja304075b

(290) Kang, Q.; Wang, T.; Li, P.; Liu, L. Q.; Chang, K.; Li, M.; Ye, J. H. *Angew. Chem. Int. Ed.* **2015,** *54*, 841. doi: 10.1002/anie.201409183

(291) Tabata, M.; Maeda, K.; Higashi, M.; Lu, D.; Takata, T.; Abe, R.; Domen, K. *Langmuir* **2010,** *26*, 9161. doi: 10.1021/la100722w